Boronated Cyanometallates

Brendon J. McNicholas*[1], Cherish Nie[1], Anex Jose[2], Paul H. Oyala[1], Michael K. Takase[1], Larry M. Henling[1], Alexandra T. Barth[1], Alessio Amaolo[1], Ryan G. Hadt[1], Edward I. Solomon[2], Jay R. Winkler[1], Harry B. Gray*[1], and Emmanuelle Despagnet-Ayoub*[3]

1. Division of Chemistry and Chemical Engineering, California Institute of Technology, 1200 East California Boulevard, Pasadena, California 91125, United States of America
2. Department of Chemistry, Stanford University, 333 Campus Drive, Stanford, California 94305, United States of America
3. Department of Chemistry, Occidental College, 1600 Campus Road, Los Angeles, California 90041, United States of America

ABSTRACT: Thirteen boronated cyanometallates $[M(CN-BR_3)_6]^{3/4/5-}$ (M = Cr, Mn, Fe, Ru, Os; BR_3 = BPh_3, $B(2,4,6,-F_3C_6H_2)_3$, $B(C_6F_5)_3$) and one metalloboratonitrile $[Cr(NC-BPh_3)_6]^{3-}$ have been characterized by X-ray crystallography and spectroscopy [UV-vis-NIR, NMR, IR, spectroelectrochemistry, and magnetic circular dichroism (MCD)]; CASSCF+NEVPT2 methods were employed in calculations of electronic structures. For $(t_{2g})^5$ electronic configurations, the lowest energy ligand-to-metal charge transfer (LMCT) absorptions and MCD C-terms in the spectra of boronated species have been assigned to transitions from cyanide π + B-C borane σ orbitals. CASSCF+NEVPT2 calculations including t_{1u} and t_{2u} orbitals reproduced $t_{1u}/t_{2u} \rightarrow t_{2g}$ excitation energies. Many $[M(CN-BR_3)_6]^{3/4-}$ complexes exhibited highly electrochemically reversible redox couples. Notably, the reduction formal potentials of all five $[M(CN-B(C_6F_5)_3)_6]^{3-}$ anions scale with LMCT energies, and Mn(I) and Cr(II) compounds, $[K(18-crown-6)]_5[Mn(CN-B(C_6F_5)_3)_6]$ and $[K(18-crown-6)]_4[Cr(CN-B(C_6F_5)_3)_6]$, are surprisingly stable. Continuous wave and pulsed electron paramagnetic resonance (hyperfine sublevel correlation) spectra were collected for all Cr(III) complexes; as expected, ^{14}N hyperfine splittings are greater for $(Ph_4As)_3[Cr(NC-BPh_3)_6]$ than for $(Ph_4As)_3[Cr(CN-BPh_3)_6]$.

Introduction

Homoleptic cyanometallates are a rich class of molecular anions that have been studied since the 18th century.[1] The first successful synthesis of potassium hexacyanoferrate(II) occurred in 1752, when Pierre Joseph Macquer cleaved the cyanide-linkage polymer Prussian Blue with hydroxide.[1] The synthesis of potassium hexacyanoferrate(III) was reported 70 years later, by Leopold Gmelin.[2] The past 200 years have witnessed a steady growth in the synthesis, characterization, and applications of homoleptic cyanometallates, with cyanide complexes of nearly every transition metal reported in the literature.[3] Most metal cyanide complexes are traditionally prepared from the reaction of alkali cyanides with metal chloride salts at elevated temperatures.[3,4] Oxidized versions of cyanometallates are typically prepared using reduced forms and a suitable oxidant.[5–8] Coordination numbers of metal cyanides vary substantially throughout the d-block.[3]

Ligand field theory along with electronic spectroscopy and other physical methods have been employed in work aimed at understanding the ground- and excited-state properties of homoleptic cyanometallates.[9] Spectroscopically relevant molecular orbitals for hexacyanoferrates are shown in **Figure 1**.[5,10] To the best of our knowledge, the first UV-visible absorption spectrum of hexacyanoferrate(III) (**Fe-III**) was reported in 1931.[11]

Serendipitously, the $^2T_{2g}$ ground state electronic structures of $[M(CN)_6]^{3-}$ (M = Fe, Ru, Os) complex anions provided a means for quantifying the magnetic circular dichroism (MCD) selection rules developed in the 1950s and 1960s by Schatz, McCaffrey, and Stephens, with important contributions later by Piepho and Kobayashi.[12–15] Neglecting effects of spin-orbit coupling, the low-temperature MCD spectra of open-shell hexacyanometallate complexes should exhibit intense, positive and negative differential absorptions of approximately equal intensities from allowed ligand to metal charge transfer (LMCT) transitions that are signed differently based on orbital parentage. Notably, the contribution of different MCD terms to the spectrum of hexacyanoferrate(III) was quantitatively assessed by Upton et al., who demonstrated that *B*-term contributions are non-negligible above 20 K, and that *C*-terms are dominant at lower temperatures, as expected for complexes with orbitally degenerate, paramagnetic ground states.[16] The MCD spectra of hexacyano-ruthenate(III) (**Ru-III**) and hexacyanoosmate(III) (**Os-III**) in frozen matrices were studied later by Kang et al., who demonstrated the striking similarity of these spectra to those of **Fe-III**, with only minor shifts in LMCT bands as a function of metal center.[17] In contrast to Group VIII complexes, the MCD spectroscopic properties of hexacyanomanganate(III/II) (**Mn-III/II**) and hexa-cyanochromate(III/II) (**Cr-III/II**) have not been as well documented, with the majority of studies aimed at applications such as building blocks for Prussian Blue-type battery materials, phosphors, single-molecule magnets.[18–21]

Energy

3a$_{1g}$

5t$_{1u}$

2t$_{2u}$ +2t$_{1g}$ + 3t$_{2g}$

4p —   4t$_{1u}$ π*

3e$_g$

4s —   2t$_{2g}$

3t$_{1u}$ + 2a$_{1g}$ σ$_2$

3d —   π
2e$_g$ +1t$_{2u}$ + 1t$_{1g}$

2t$_{1u}$ σ$_1$

1e$_g$

1t$_{2g}$ +1t$_{1u}$

1a$_{1g}$
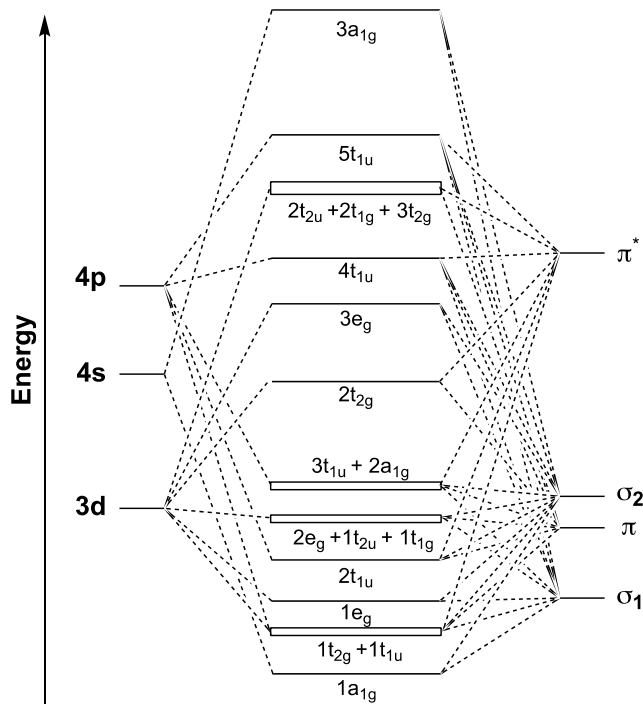
Figure 1. Molecular orbital energy level diagram for hexacyanometallates. Adapted from reference [5].

Many cyanometallates exhibit electrochemically reversible redox couples. In the 1970s, Gutmann et al. published detailed studies that included determination of the formal potentials of **Fe-III/II** and **Mn-IV/III/II** in a variety of protic and aprotic solvents.[22–24] His studies demonstrated that both **Fe-III/II** and **Mn-IV/III/II** potentials exhibit a dramatic solvent dependence, as set out for the former complex in **Table 1**. Of interest is that an approximately linear correlation exists between the formal potential of the **Fe-III/II** redox couple and the acceptor number of the solvent. Importantly, these studies led to a better understanding of the effects of both dielectric constant and donor-acceptor interactions on the ground-state electronic properties of cyanometallates while simultaneously providing a unifying theory for effects of donor-acceptor interactions of solvents on the reactivity of small molecules. The Gutmann donor-acceptor model, as one method of quantifying the effects of Lewis acidity and basicity, has been supported by solvent-dependence studies of both chemical and electrochemical reactions. Acceptor number values are measured by finding the ^{31}P-NMR shift of triethyl-phosphine oxide (Et$_3$PO) with antimony pentachloride in 1,2-dichloroethane (arbitrarily set to AN = 100), where a solvent with high electrophilicity inductively withdraws electron density through the Et$_3$PO oxygen.[25]

Table 1. Formal potentials for (TBA)$_3$[Fe(CN)$_6$] (**Fe-III**) in aprotic and protic solvents with varying dielectric constants and acceptor numbers. Voltammetry was acquired with 0.1 M TBAClO$_4$ as electrolyte. Data from references [22],[24],[26],[27].

Solvent	$E^{0'}$ (V vs. Fc$^{+/0}$)	ε	AN
N-Methylpyrrolidinone	−1.75	32.0	13.3
N,N-Dimethylformamide	−1.72	36.1	16.0
Acetonitrile	−1.54	38.0	18.9
Dimethylsulfoxide	−1.51	45.0	19.3
N,N-Dimethylthioformamide	−1.48	51.2	18.8
1,2-Dichloroethane	−1.43	10.1	16.7
Propylene carbonate	−1.32	69.0	18.3
Nitromethane	−1.26	35.9	20.5
Ethanol	−0.88	24.3	37.9
Methanol	−0.74	32.6	41.5
Acetic acid	0.15	6.2	52.9

Lewis acid-base interactions, ranging from frustrated Lewis pairs to solvent effects to full dative bond formation, have been exploited in numerous applications. For example, in cyanometallates, boranes are neutral Lewis acids that will coordinate to the lone pair of nitrogen in a dative bond when the carbon lone pair is already coordinated to a metal. According to electronic structure calculations, coordination of an electron-deficient species to nitrogen lowers all molecular orbital levels, but not by the same amount.[28] When solvation effects are minimized, anodic shifts in formal potentials are consistent with the relative Lewis acidity of electron acceptors, as evidenced by work on borane adducts of Fe(phen)$_2$(CN)$_2$.[29] Adding methyl cation to a cyanide nitrogen provides an extreme example of Lewis acidity effects, as the electronic structures of metal-methylisocyanide complexes are much like those in which metals are ligated by carbon monoxide.[30] Indeed, methylation dramatically alters the electronic structures of cyanometallates, and in most cases metal-to-ligand charge-transfer (MLCT) transitions are blue shifted to the point that the lowest energy absorptions are ligand-centered.[30,31]

Many investigators have studied the effects of Lewis acid to ligand coordination on the properties of transition metal complexes.[32–34] The first example of borane coordination to cyanometallates was reported by Duward Shriver in 1962. In this study, he provided IR spectroscopic evidence for BF$_3$ coordination to K$_2$Ni(CN)$_4$, K$_4$Fe(CN)$_6$, and K$_4$Mo(CN)$_8$.[35] Although these adducts were not

stable in aprotic and protic solvents, the N-B bond in vacuum was shown to be quite strong, as evidenced by low-pressure experiments.[35] Another important finding from this work was the blueshift in the CN stretching frequency upon boronation. Note that Gutmann, in his original publications, mentioned the instability of the **Fe-III** BF_3 adduct, despite the success that Shriver experienced with boronation of **Fe-II**.[22]

Soon after, in 1963, Shriver extended BF_3 coordination to a heteroleptic cyanometallate, $Fe(phen)_2(CN)_2$, where a color change was attributed to a blueshift in the MLCT absorption of the complex.[36] Extending these studies even further in 1966, Shriver and Posner demonstrated that shifts in IR frequencies and charge-transfer bands of $Fe(phen)_2(CN)_2$ adducts could be related to the Lewis acidity of the borane.[37] This study reported the first example of the effects of neutral Lewis acids on the formal potentials of transition metal complexes, with BBr_3 exerting a more dramatic shift than BF_3, in accord with the stronger Lewis acidity of BBr_3. Later, in the 1980s, Woodcock and Shriver demonstrated Lewis acid coordination to $CpFe(CO)_2CN$ and $Fe(phen)_2(CN)_2$ in acidic molten salts.[29] In an $AlCl_3$ melt, $Fe(phen)_2(CN)_2$ exhibited dramatic color changes along with blueshifted CN stretching frequencies and MLCT transition maxima.

After a period of greatly reduced research activity on the incorporation of boranes into cyanometallates, Bochmann et al. reported that $B(C_6F_5)_3$ (BCF) adducts of tetracyanonickelate(II) and tetracyanopalladate(II) functioned as non-coordinating anions in metallocene-catalyzed polymerizations.[38] Beyond non-coordinating anions and Lewis acid coordination effects on spectroscopic properties, Schelter and Dunbar et al. reported that coordination of BPh_3 to hexacyanochromate(III) (**Cr-III**) at elevated temperatures resulted in isomerization of cyanoboratochromate (M-CN-BR$_3$) to the thermodynamic product, boratonitrile-chromate (M-NC-BR$_3$).[39] And, in a series of papers, Ko and coworkers demonstrated that Lewis-acid coordination affects formal potentials and the luminescence behavior of heteroleptic cyanometallates. Notably, these investigators reported that BCF adducts of $Re(R_2phen)(CO)_3(CN)$ exhibit improved quantum yields and electrochemical properties relative to the parent complexes.[40] These reports were followed by work on $Os(bpy)_2(CN)_2$ and its derivatives with BPh_3 and BCF.[41] In addition, Ko also confirmed that boronation blueshifts MLCT absorptions and increases excited-state lifetimes of heteroleptic cyanometallates. Notably, boronation also has similar effects on the spectroscopic and photophysical

properties of heteroleptic Ir(III) and Cu(I) diimine complexes.[42,43] Of interest is that BCF/BPh₃ adducts of heteroleptic Re(I) diimine carbonyls have shown promise as selective sensors for cyanide anion.[44] Also, Wenger et al. have boronated heteroleptic Ru(II) and Ir(III) diimine complexes and demonstrated their high activity for energy transfer and photoredox catalysis.[45,46] Most recently, Wenger et al. have provided a comprehensive study of the electronic structural properties of Fe(II) boronated cyanometallates as a function of the number of cyanide ligands.[47]

Studies of cyanometallates have been driven by the promise of applications in magnetic materials involving single-molecule/Prussian-Blue analogues and in electrode materials for solid-state batteries.[18,48–50] Of direct relevance to our research is the performance of reversible cyanometallates as electrolytes in redox flow batteries. For example, Marshak et al. have shown the viability of **Fe-III/II** as a redox-active electrolyte pair for long-lived charge-discharge cycling when coupled with 2,6-dihydroxyanthraquinone.[51] More recently, a study of ammonium hexacyanoferrate(II) with viologen derivatives as anolytes demonstrated that high energy density can be achieved with cyanometallate flow batteries.[52]

In 2019, we reported that the **Fe-III/II** formal potential is increased over 2.1 V in the BCF adduct.[53] Additionally, through voltammetry experiments, we have shown that voltage differences between metal-based and ligand-based redox couples can be dramatically increased in heteroleptic cyanide complexes of both iron and ruthenium, thereby improving overall cell voltages for symmetric redox flow batteries.[54] Additionally, significant improvements in quantum yields and lifetimes of Ru(II) complexes occur upon boronation.[55]

We have extended our work on boronated cyanides to include syntheses and full characterization of 13 homoleptic boronated cyanometallates $[M(CN-BR_3)_6]^{3/4/5-}$ (M = Cr, Mn, Fe, Ru, Os; BR_3 = BPh_3, $B(2,4,6,-F_3C_6H_2)_3$, $B(C_6F_5)_3$) and one boratonitrile $[Cr(NC-BPh_3)_6]^{3-}$. More specifically, using a combination of room-temperature UV-vis-NIR and low-temperature MCD spectroscopy, we have demonstrated that boronation results in new LMCT transitions that arise from B-C σ-bonding orbital contributions to C-N π orbitals in homoleptic cyanometallates. In addition, we report that the formal potentials of the boronated complexes are shifted by 2.08–2.29 V relative to the parents. Because of these anodic shifts, the characterization of **Mn-II-BCF**, **Mn-I-BCF**, and **Cr-II-BCF**,

as well as electrochemically generated **Cr-I-BCF** was possible. Continuous-wave (CW) electron paramagnetic resonance (EPR) spectra of **Cr/Fe/Ru/Os-III-BCF** and hyperfine sublevel correlation (HYSCORE) spectra of (Ph$_4$As)$_3$[Cr(CN-BPh$_3$)$_6$] (**Cr-III-CN-BPh$_3$**) and (Ph$_4$As)$_3$[Cr(NC-BPh$_3$)$_6$] (**Cr-III-NC-BPh$_3$**) are also reported. Dramatic changes in ^{14}N ($I = 1$) hyperfine coupling constants in **Cr-III-CN-BPh$_3$** and **Cr-III-NC-BPh$_3$** provide conclusive evidence of the primary coordination environment of the chromium center. And, in our theory work, we have exploited a descent in symmetry approach to correlate *ab initio* calculations with experimental spectra.

We suggest that the unique electronic structural and electrochemical properties of these adduct complexes could lead to applications in electrocatalysis, as well as in the design of new flow battery architectures, molecular magnets, and qubits.[56] Since boronation blueshifts ligand field and MLCT transitions while variably shifting LMCT transitions, selective ligand modifications could lead to longer-lived excited states in complexes of earth-abundant transition metal ions.

**Synthesis and X-Ray Crystallography**
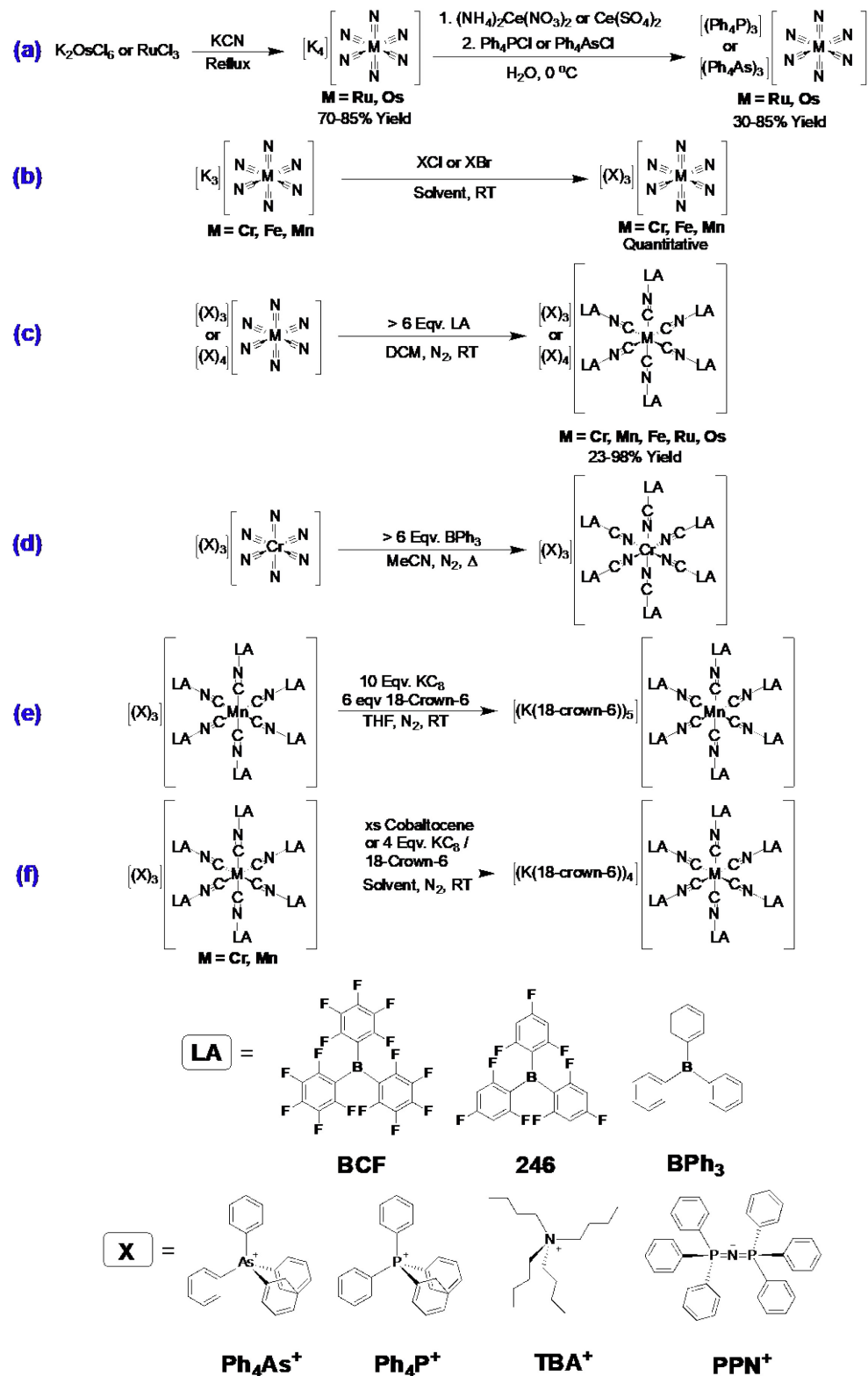
Figure 2. Reaction schemes for generation of parent and boronated cyanometallates. **(a)** Synthesis of $(X)_3[Ru(CN)_6]$ and $(X)_3[Os(CN)_6]$ (**Ru-III** and **Os-III**). **(b)** Synthesis of $(X)_3[Cr(CN)_6]$, $(X)_3[Mn(CN)_6]$, and $(X)_3[Fe(CN)_6]$ (**Cr-III**, **Mn-III**, and **Fe-III**). **(c)** Synthesis of boronated derivatives of hexacyanometallate complexes. **(d)** Synthesis of $(X)_3[Cr(NC-BPh_3)_6]$ (**Cr-III-NC-BPh₃**). **(e)** Synthesis of $[K(18\text{-crown-}6)]_5[Mn(CN-B(C_6F_5)_3)_6]$ (**Mn-I-BCF**). **(f)** Synthesis of $[K(18\text{-crown-}6)]_4[Cr(CN-B(C_6F_5)_3)_6]$ (**Cr-II-BCF**).

The syntheses of boronated cyanometallates are given in **Figure 2**. Previous studies provided starting points for syntheses of potassium hexacyanoruthenate(II), $K_4[Ru(CN)_6]$, and potassium hexacyanoosmate(II), $K_4[Os(CN)_6]$, from ruthenium(III) trichloride and potassium hexachloroosmate(IV), respectively.[7,57] The yield of $K_4[Os(CN)_6]$ was increased to nearly 80% by refluxing under an inert atmosphere (**Figure 2(a)**). Tetrabutylammonium (TBA^+) salts of Fe(II), Ru(II), and Os(II) were generated by forming the acid salts in hydrochloric acid from $K_4[M(CN)_6]$, followed by titration with TBAOH and extensive drying of the resulting $(TBA)_4[M(CN)_6]$.[58]

To generate Os(III) and Ru(III) salts, $K_4[Os(CN)_6]$ was oxidized with one equivalent of ceric ammonium nitrate, and $K_4[Ru(CN)_6]$ was oxidized in the dark with one equivalent of ceric sulfate ($Ce(SO_4)_2$), both at 0 °C. Solutions were treated with excess tetraphenylarsonium chloride (Ph_4AsCl) or tetraphenylphosphonium chloride (Ph_4PCl) to precipitate the lipophilic salts, which were washed with cold water and dried under vacuum (**Figure 2(b)**).[6,8,59] An alternative synthetic route employed a biphasic mixture of the potassium salt of Os(II) or Ru(II) in H_2O and tetrabutylammonium chloride (TBACl), bis(triphenylphosphine)iminium chloride (PPNCl), Ph_4PCl, or Ph_4AsCl in dichloromethane (CH_2Cl_2) in the dark at 0 °C with the addition of stoichiometric $Ce(SO_4)_2$.[60]

TBA^+ salts of **Fe-III** and **Cr-III** were synthesized by standard literature procedures.[61,62] The PPN^+, Ph_4P^+, and Ph_4As^+ salts of **Fe-III** and **Cr-III** were synthesized in aqueous solution by combining a slight stoichiometric excess of PPNCl, Ph_4PCl, or Ph_4AsCl with $K_3[Fe(CN)_6]$ or $K_3[Cr(CN)_6]$, then filtering, washing with distilled water, and drying overnight *in vacuo* (**Figure 2(b)**). Lipophilic salts of hexacyanomanganate(III) were synthesized under nitrogen by stirring an excess of TBACl, PPNCl, Ph_4PCl, or Ph_4AsCl with $K_3[Mn(CN)_6]$ overnight in MeCN, filtering to remove unreacted solid, and precipitating the product with diethyl ether (Et_2O) (**Figure 2(b)**).

Synthesis of Homoleptic Boronated Cyanometallates.
Boronation with **BCF** of the **Fe-III**, **Ru-III**, **Os-III**, **Cr-III** (also **BPh₃**), and **Mn-III** (also tris(2,4,6-trifluorophenyl)borane (**246**)) salts in dichloromethane (DCM) resulted in dramatic color changes from yellow or orange to violet for Fe(III) (**Fe-III-BCF**), to green for Ru(III) (**Ru-III-BCF**), to indigo for Os(III) (**Os-III-BCF**), to colorless or lemon yellow for Cr(III) (**Cr-III-**

9

BCF/Cr-III-CN-BPh₃), and to orange-red or yellow for Mn(III) (**Mn-III-BCF/Mn-III-246**) (**Figure 2(c)**).

Ru-III-BCF and **Os-III-BCF** were reduced by diethyl ether (Et₂O) or tetrahydrofuran (THF) in solutions of the salt in DCM, followed by precipitation of the colorless product by addition of more Et₂O (**Ru-II-BCF** and **Os-II-BCF**). Alternatively, TBA⁺ salts of **Fe-II**, **Ru-II**, and **Os-II** were boronated in a 1:1 mixture of DCM:toluene, precipitated as oils with excess toluene, dried, and purified by redissolving in MeCN and precipitating with Et₂O to obtain the boronated M(II) species (**Figure 2(c)**). X-ray quality crystals of **Fe/Ru/Os-II-BCF** complexes were grown from concentrated solutions in DCM with minimal Et₂O at −20 °C. All **M-III-BCF/BPh₃** complexes were crystallized from concentrated DCM solutions at −20 °C.

Additionally, we successfully isolated and fully characterized the reduced compounds, [K(18-crown-6)]₄[Cr(CN-B(C₆F₅)₃)₆] (**Cr-II-BCF**), (TBA)₄[Mn(CN-B(C₆F₅)₃)₆] (**Mn-II-BCF**), and (TBA)₄[Mn(CN-2,4,6-BArF₉)₆] (**Mn-II-246**), and partially characterized the reduced species [K(18-crown-6)]₅[Mn(CN-B(C₆F₅)₃)₆] (**Mn-I-BCF**). Use of either a four-fold excess of potassium graphite (KC₈) ($E^{0'} \sim -2.6$ V vs. Fc⁺/⁰)[63] with a four-fold excess of 18-crown-6 ether in THF or excess cobaltocene in DCM followed by cooling at −25 °C afforded crystalline salts of **Cr-II-BCF** (**Figure 2(f)**). **Mn-II-BCF** and **Mn-II-246** were formed by one electron reduction of **Mn-III-BCF/246** by either excess cobaltocene in DCM or excess KC₈ and 18-crown-6 ether in THF followed by addition of DCM (**Figure 2(f)**). Crystallization was achieved by cooling THF solutions to −25 °C. Furthermore, **Mn-I-BCF** was obtained by reduction of **Mn-III-BCF** in THF with a ten-fold excess of KC₈ and a six-fold excess of 18-crown-6 ether. The solution was decanted and cooled to −25 °C, resulting in the formation of garnet red crystals of **Mn-I-BCF** (**Figure 2(e)**).

To compare the effects of ligand field strength on the electronic structures of cyanometallates, we synthesized the linkage isomer (TBA)₃[Cr(NC-BPh₃)₆] (**Cr-III-NC-BPh₃**) (N-bound cyanides are strong σ-donors and weak π-acceptors).[39,64] When **Cr-III** was refluxed with BPh₃ in MeCN, a dramatic color change from pale yellow to orange-red occurred.[39] Remarkably, the reaction triggered inversion of all six cyanide ligands, affording a hexakis-boratonitrile complex (**Figure 2(d)**). Infrared and UV-vis spectra along with an X-ray structure analysis supported assignment of N-

ligation in **Cr-III-NC-BPh₃**. Note that Figgis and coworkers employed neutron diffraction to confirm C-bonding in the inner coordination sphere of hexacyanochromate(III).[65]

Of interest are the spectroscopic and electronic structural differences between cyanoborate (M-CN-BR₃) and boratonitrile (M-NC-BR₃) complexes. Based on our success in synthesizing **Cr-III-BCF** in DCM (a weakly Lewis basic solvent) and calculations suggesting that the energies of thermodynamic **Cr-III-NC-BPh₃** and kinetic **Cr-III-CN-BPh₃** products are similar, we attempted synthesis and crystallographic characterization of the C-bound isomer. Addition of a stoichiometric excess of BPh₃ to a room-temperature solution of **Cr-III** in DCM resulted in an immediate color change from pale yellow to lemon yellow. The solution was concentrated by evaporating solvent *in vacuo*, and the oil was placed in a freezer at -20 $^{\circ}$C (**Figure 2(d)**). Structural characterization of the yellow crystals revealed C-ligation, **Cr-III-CN-BPh₃**. We found that after prolonged exposure to X-rays, the color of the crystal changed to an orangish pink, suggesting inversion of ligation had occurred (we used early reflections for structure refinement).

Selected bond lengths for parent and boronated cyanometallates are presented in **Tables 2**, **3**, and **4**. Structures of **Mn-I-BCF** and **Cr-II-BCF** are shown in **Figure 3**; and those of **Fe-III-BCF, Ru-III-BCF, Os-III-BCF, Cr-III-BCF, Cr-III-CN-BPh₃**, and **Cr-III-NC-BPh₃** in **Figure 4**. Upon boronation, a descent in symmetry from O_h to D_{3d} occurs, assuming trigonal symmetry for staggered boranes. We previously showed that the M-C bond lengths display slight decreases based on the Lewis acidity of the borane.[53] For example, **Cr-III-CN-BPh₃** and **Cr-III-BCF** have similar average M-C bond lengths (2.068 Å and 2.065 Å, respectively**).** The M-C bond lengths for the complexes generally increase in the order,

$$M(I) < M(II)\text{-BCF} < M(II) < M(III)\text{-BCF} < M(III)$$
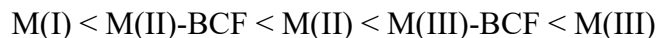
which is a trend based on the interplay between metal oxidation state and borane Lewis acidity. Decreasing metal oxidation state increases the number of electrons available for π-backbonding, thereby increasing M-C covalency. Increasing the N-dative interaction with the borane decreases M-C σ-covalency and increases π-backbonding. These data conclusively demonstrate that backbonding interactions in metal cyanoborates dramatically affect M-C bonding.

In contrast, there are only very minor changes in C-N bond lengths. For example, **Fe-III-BCF** shows a slight increase in average C-N bond length relative to **Fe-III** (1.155 Å vs. 1.139 Å, respectively), whereas for **Os-III-BCF**, there is a slight C-N shortening relative to **Os-III** (1.127 Å vs. 1.145 Å).

Mn-I-BCF and **Fe-II-BCF** have the shortest average M-C bonds (1.909 Å and 1.900 Å, respectively) in the series. For comparison, previous studies of $[Mn(CO)_6](BF_4)$ revealed an average Mn-C bond length of 1.905 Å, nearly identical with those obtained for Mn(I) and Fe(II) in our work.[66] It is well known that carbonyl and cyanide ligand fields are very strong in complexes with d^5 and d^6 metal valence electrons, owing to enhanced π-backbonding. In contrast, ligand field strengths are weaker in d^3 **Cr-III-CN-BPh₃** and **Cr-III-NC-BPh₃**, with longer average M-C/N bond lengths (2.068 Å and 2.004 Å, respectively), in accord with greatly decreased backbonding in low d-count complexes.[67–69]

Table 2. Selected bond lengths for cyanometallate(II) complexes.

Bond (Å) / Compound	(TEA)₄[Fe(CN)₆][a] / (TBA)₄[Fe(CN-BCF)₆]	Na₄[Ru(CN)₆][b] / (Ph₄P)₄[Ru(CN-BCF)₆]	Na₄[Os(CN)₆][b] / (Ph₄As)₄[Os(CN-BCF)₆]	(TBA)₄[Mn(CN-BCF)₆] / (PPN)₄[Mn(CN-246)₆]
M-C₁ (or C₁ #1)	1.926(5) / 1.899(4)	2.035(3) / 2.0220(11)	2.068(7) / 2.023(5)	1.975(6) / 1.955(2)
M-C₂ (or C₁ #2)	1.920(4) / 1.899(4)	2.023(3) / 2.0220(11)	2.044(7) / 2.023(5)	1.975(6) / 1.955(2)
M-C₃ (or C₂ #1)	1.922(5) / 1.904(3)	2.010(3) / 2.0026(11)	2.013(6) / 2.037(5)	1.949(6) / 1.958(2)
M-C₄ (or C₂ #2)	1.924(4) / 1.904(3)	2.035(3) / 2.0027(11)	2.068(7) / 2.037(5)	1.949(6) / 1.958(2)
M-C₅ (or C₃ #1)	1.919(4) / 1.897(3)	2.023(3) / 2.0152(12)	2.044(7) / 2.036(5)	1.935(6) / 1.955(2)
M-C₆ (or C₃ #2)	1.918(4) / 1.897(3)	2.010(3) / 2.0152(12)	2.013(6) / 2.036(5)	1.935(6) / 1.955(2)
C-N₁	1.174(6) / 1.146(4)	1.151(4) / 1.1546(13)	1.116(9) / 1.144(6)	1.157(7) / 1.153(3)
C-N₂	1.164(6) / 1.146(4)	1.158(5) / 1.1546(13)	1.156(9) / 1.144(6)	1.157(7) / 1.153(3)
C-N₃	1.168(6) / 1.152(4)	1.161(4) / 1.1551(13)	1.149(9) / 1.148(6)	1.164(7) / 1.150(3)
C-N₄	1.170(6) / 1.152(4)	1.151(4) / 1.1551(13)	1.116(9) / 1.148(6)	1.164(7) / 1.150(3)

C-N₅	1.161(5) / 1.160(4)	1.158(5) / 1.1530(14)	1.156(9) / 1.133(7)	1.162(7) / 1.155(3)
C-N₆	1.156(6) / 1.160(4)	1.161(4) / 1.1530(14)	1.149(9) / 1.133(7)	1.162(7) / 1.155(3)

[a]Reference [53] [b]Reference [70]

Table 3. Selected bond lengths for cyanometallate(III) complexes.

Bond (Å) / Compound	(TEA)₃[Fe(CN)₆][a] / (PPN)₃[Fe(CN-B(C₆F₅)₃)₆]	(Ph₄As)₃[Ru(CN)₆][b] / (Ph₄P)₃[Ru(CN-B(C₆F₅)₃)₆]	(Ph₄P)₃[Os(CN)₆][c] / (Ph₄P)₃[Os(CN-B(C₆F₅)₃)₆]	(PPN)₃[Mn(CN)₆][d] / (PPN)₃[Mn(CN-B(C₆F₅)₃)₆]	(PPN)₃[Mn(CN-B(246-F₃C₆H₂)₃)₆]
M-C₁ (or C₁ #1)	1.935(5) / 1.918(8)	2.066(6) / 2.025(9)	2.063(5) / 2.066(11)	2.022(2) / 1.9989(19)	1.9749(13)
M-C₂ (or C₁ #2)	1.959(5) / 1.918(8)	2.064(6) / 2.025(9)	2.063(5) / 2.043(9)	2.022(2) / 1.9900(19)	1.9750(13)
M-C₃ (or C₂ #1)	1.946(8) / 1.944(9)	2.023(6) / 2.048(6)	2.070(5) / 2.060(11)	2.025(2) / 1.9768(18)	1.9794(13)
M-C₄ (or C₂ #2)	1.965(8) / 1.944(9)	2.025(6) / 2.048(6)	2.070(5) / 2.051(9)	2.025(2) / 1.983(2)	1.9794(13)
M-C₅ (or C₃ #1)	1.955(8) / 1.901(7)	2.054(6) / 2.017(8)	2.056(5) / 2.077(9)	2.013(2) / 2.0048(18)	1.9714(11)
M-C₆ (or C₃ #2)	1.959(8) / 1.902(7)	2.064(6) / 2.017(8)	2.056(5) / 2.038(10)	2.013(2) / 1.9878(18)	1.9715(11)
C-N₁	1.156(7) / 1.152(10)	1.161(6) / 1.158(9)	1.137(6) / 1.117(14)	1.161(2) / 1.138(3)	1.1498(14)
C-N₂	1.136(7) / 1.152(10)	1.143(6) / 1.158(9)	1.141(6) / 1.140(13)	1.161(2) / 1.134(2)	1.1498(14)
C-N₃	1.141(11) / 1.130(11)	1.145(6) / 1.134(9)	1.139(6) / 1.136(14)	1.161(2) / 1.142(2)	1.1508(14)
C-N₄	1.134(11) / 1.130(11)	1.165(7) / 1.134(9)	1.154(6) / 1.125(13)	1.161(2) / 1.135(3)	1.1508(14)
C-N₅	1.131(11) / 1.185(10)	1.142(6) / 1.161(9)	1.145(6) / 1.102(13)	1.156(2) / 1.142(2)	1.1489(13)
C-N₆	1.140(10) / 1.185(10)	1.147(6) / 1.161(9)	1.157(6) / 1.145(14)	1.156(2) / 1.141(2)	1.1489(13)

[a]Reference [71] [b]Reference [8] [c]Reference [6] [d]Reference [72]

Table 4. Selected bond lengths for Cr(III), Cr(II), and Mn(I) cyanometallates.

Bond (Å) / Compound	(PPh₄)₃[Cr(CN)₆][a] / (PPN)₃[Cr(CN-B(C₆F₅)₃)₆]	(Ph₄As)₃[Cr(CN-BPh₃)₆]	(Ph₄As)₃[Cr(NC-BPh₃)₆]	Na₄[Cr(CN)₆][b] / [K(18-crown-6)]₄[Cr(CN-B(C₆F₅)₃)₆]	[K(18-crown-6)]₅[Mn(CN-B(C₆F₅)₃)₆]
M-C₁ (or C₁ #1)	2.0865(19) / 2.067(4)	2.081(3)	1.995(7)	2.037(6) / 2.035(3)	1.907(3)
M-C₂ (or C₁ #2)	2.0768(19) / 2.055(4)	2.068(3)	2.009(7)	2.065(6) / 2.039(2)	1.912(3)
M-C₃ (or C₁ #3)	2.0751(18) / 2.073(4)	2.052(3)	2.002(7)	2.057(6) / 2.032(3)	1.914(3)
M-C₄ (or C₂ #1)	2.0854(18) / 2.067(4)	2.074(3)	2.011(7)	2.037(6) / 2.035(3)	1.907(3)
M-C₅ (or C₂ #2)	2.0871(18) / 2.055(4)	2.054(3)	2.008(7)	2.065(6) / 2.039(2)	1.912(3)
M-C₆ (or C₂ #3)	2.0823(18) / 2.073(4)	2.080(3)	2.003(7)	2.057(6) / 2.032(3)	1.914(3)
C-N₁	1.156(2) / 1.148(5)	1.145(3)	1.141(10)	1.155(8) / 1.149(3)	1.166(4)
C-N₂	1.149(3) / 1.143(5)	1.145(3)	1.137(10)	1.163(8) / 1.151(3)	1.169(4)

C-N₃	1.149(2) / 1.149(5)	1.145(4)	1.144(9)	1.150(8) / 1.152(3)	1.163(4)
C-N₄	1.152(2) / 1.148(5)	1.143(3)	1.152(10)	1.155(8) / 1.149(3)	1.166(4)
C-N₅	1.152(2) / 1.143(5)	1.150(4)	1.136(9)	1.163(8) / 1.151(3)	1.169(4)
C-N₆	1.154(2) / 1.149(5)	1.144(3)	1.152(10)	1.150(8) / 1.152(3)	1.163(4)

[a]Reference [73]. [b]Reference [74]
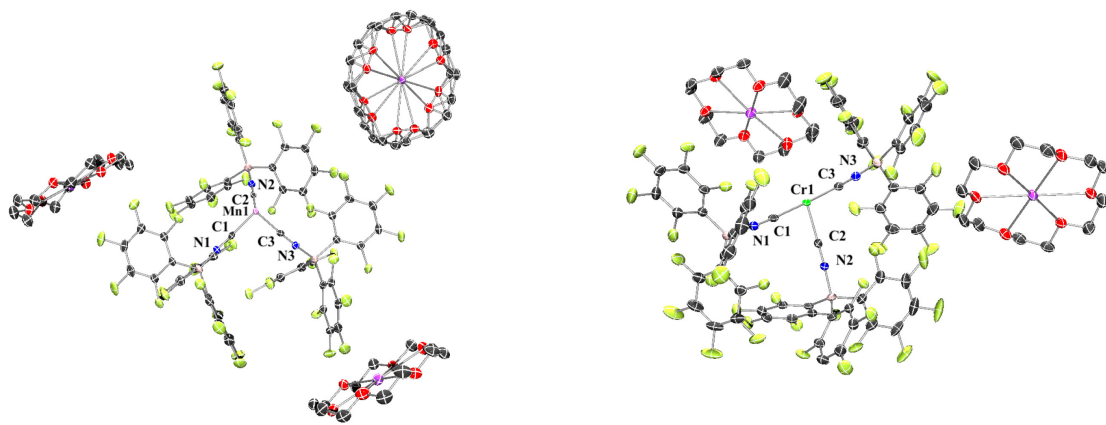
Figure 3. (**Left**) Molecular structure of [K(18-crown-6)]$_5$[Mn(CN-B(C$_6$F$_5$)$_3$)$_6$] (**Mn-I-BCF**) (One-half of a crown ether from an additional asymmetric unit was added for completeness). (**Right**) Molecular structure of [K(18-crown-6)]$_4$[Cr(CN-B(C$_6$F$_5$)$_3$)$_6$] (**Cr-II-BCF**). Displacement ellipsoids set at 50% probability, and solvent molecules and hydrogens were omitted for clarity. Structures depict the asymmetric unit for each complex.
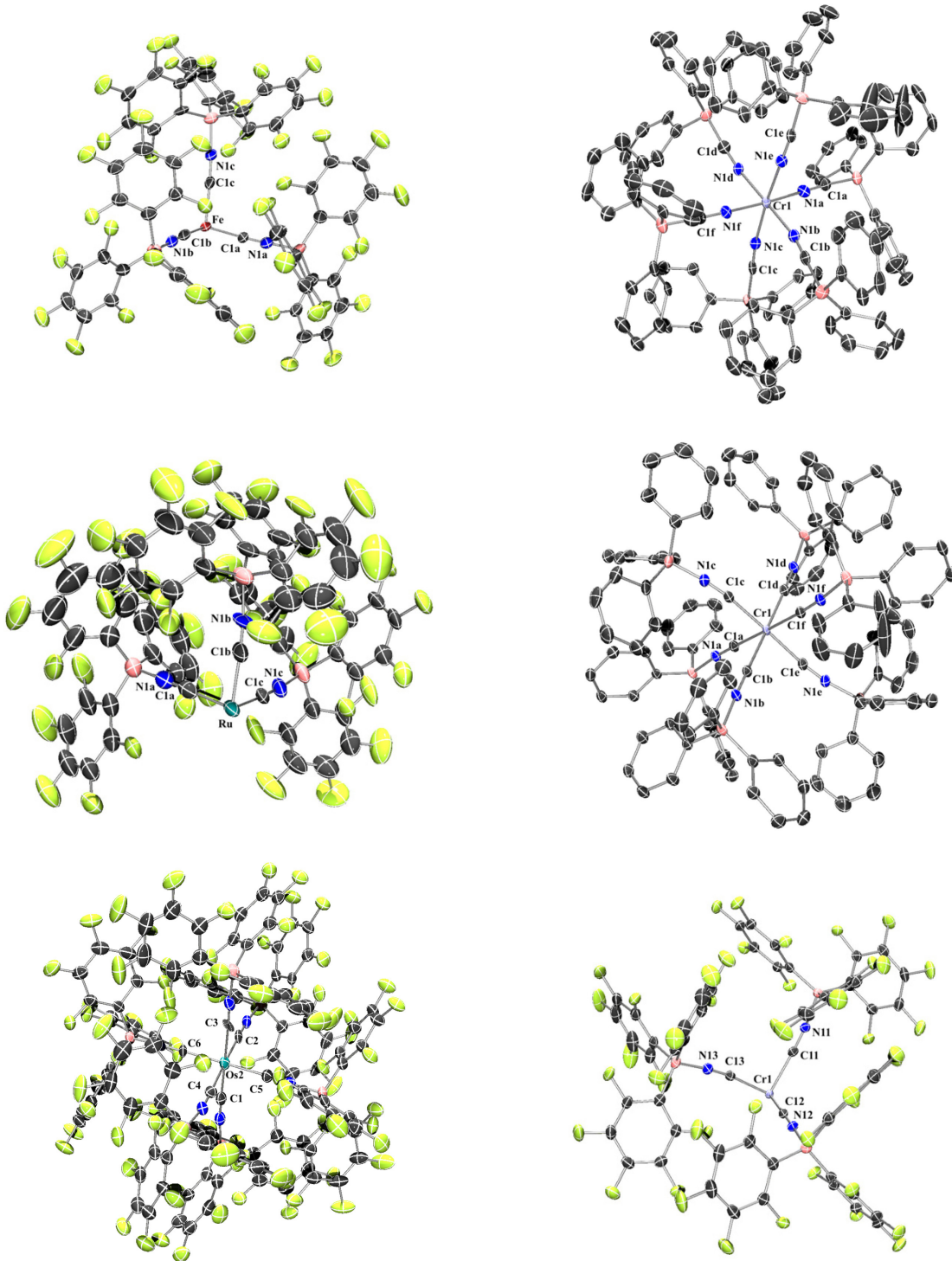
Figure 4. (**Left**) Molecular structures of (PPN)$_3$[Fe(CN-B(C$_6$F$_5$)$_3$)$_6$] (**Fe-III-BCF**), (Ph$_4$P)$_3$[Ru(CN-B(C$_6$F$_5$)$_3$)$_6$] (**Ru-III-BCF**), and (Ph$_4$P)$_3$[Os(CN-B(C$_6$F$_5$)$_3$)$_6$] (**Os-III-BCF**). (**Right**) Molecular structures of (Ph$_4$As)$_3$[Cr(NC-BPh$_3$)$_6$] (**Cr-III-NC-BPh$_3$**), (Ph$_4$As)$_3$[Cr(CN-BPh$_3$)$_6$] (**Cr-III-CN-BPh$_3$**), and (PPN)$_3$[Cr(CN-B(C$_6$F$_5$)$_3$)$_6$] (**Cr-III-BCF**). Structures depict the asymmetric unit for each complex. Displacement ellipsoids set at 50% probability, and solvent molecules, cations, and hydrogens were omitted for clarity.

IR and NMR Spectroscopy

IR v(CN) data are given in **Table 5**. Across all complexes, an average increase of 120 cm^{-1} in cyanide stretching frequency was observed when comparing parent and BCF anions [e.g., v(CN): **Ru-III**, 2090; **Ru-III-BCF**: 2210 cm^{-1}]. The differences are attributed to the greater effect of σ-donation from cyanide to borane relative to π-backdonation from metal to cyanide. We suggest that π-backdonation plays a key role in the variation of vibrational frequencies as a function of oxidation state (**Mn-III-BCF**: 2222; **Mn-II-BCF**: 2151, **Mn-I-BCF**: 2041 cm^{-1}). Also of interest is that v(CN) is higher in **Cr-III-BCF** (2229) than in **Cr-III-BPh₃** (2202 cm^{-1}).

^{11}B NMR chemical shifts for boronated cyanometallates are given in **Table 6**. As more electron density is transferred to boron through dative bonding, chemical shifts move upfield. As expected for d^6 diamagnetic complexes, **Fe/Ru/Os-II-BCF** ^{11}B NMR chemical shifts are similar (~ −14 ppm), whereas paramagnetic compounds show a distinct upfield trend [**Fe-III-BCF** (-54.2 ppm), **Os-III-BCF** (−37.6 ppm), **Mn-II-BCF** (−60.4 ppm), and **Mn-III-BCF** (−136.1 ppm)]. Dramatic shifts in ^{11}B NMR signals are to be expected. For example, Fe(III) boron cluster cage compounds exhibit upfield chemical shifts, in one case to −451.1 ppm, while a diamagnetic Co(III) analogue shifts downfield (+6.5 ppm).[75]

Table 5. IR data: CN stretching frequencies (solid samples).

Complex	Abbreviation	v_{CN} (cm^{-1})
(TBA)₃[Fe(CN)₆][a]	**Fe-III**	2095
(TEA)₄[Fe(CN)₆]	**Fe-II**	2012
(TBA)₃[Fe(CN-B(C₆F₅)₃)₆]	**Fe-III-BCF**	2228
(TBA)₄[Fe(CN-B(C₆F₅)₃)₆]	**Fe-II-BCF**	2165
(TBA)₃[Ru(CN)₆][a]	**Ru-III**	2090
(TBA)₄[Ru(CN)₆][a]	**Ru-II**	2060
(TBA)₃[Ru(CN-B(C₆F₅)₃)₆]	**Ru-III-BCF**	2210
(TBA)₄[Ru(CN-B(C₆F₅)₃)₆]	**Ru-II-BCF**	2172
(PPh₄)₃[Os(CN)₆][b]	**Os-III**	2100
K₄[Os(CN)₆][c]	**Os-II**	2032
(PPh₄)₃[Os(CN-B(C₆F₅)₃)₆]	**Os-III-BCF**	2204
(PPh₄)₄[Os(CN-B(C₆F₅)₃)₆]	**Os-II-BCF**	2152
(PPN)₃[Mn(CN)₆][d]	**Mn-III**	2095
(PPN)₂[Mn(CN)₆][d]	**Mn-IV**	2132
(TBA)₃[Mn(CN-B(C₆F₅)₃)₆]	**Mn-III-BCF**	2222
(TBA)₄[Mn(CN-B(C₆F₅)₃)₆]	**Mn-II-BCF**	2151
(PPN)₅[Mn(CN-B(C₆F₅)₃)₆]	**Mn-I-BCF**	2041
(TBA)₃[Mn(CN-2,4,6-BArF₉)₆]	**Mn-III-246**	2226
(TBA)₄[Mn(CN-2,4,6-BArF₉)₆]	**Mn-II-246**	2148
(TEA)₃[Cr(CN)₆][e]	**Cr-III**	2109
K₄[Cr(CN)₆][f]	**Cr-II**	2022
(TBA)₃[Cr(CN-B(C₆F₅)₃)₆]	**Cr-III-BCF**	2229
(TBA)₄[Cr(CN-B(C₆F₅)₃)₆]	**Cr-II-BCF**	2149
(Ph₄As)₃[Cr(CN-BPh₃)₆]	**Cr-III-CN-BPh₃**	2202
(Ph₄As)₃[Cr(NC-BPh₃)₆]	**Cr-III-NC-BPh₃**	2211

[a]Reference [59] [b]Reference [6] [c]Reference [76] [d]Reference [77] [e]Reference [39] [f]Reference [78]

Table 6. ^{11}B NMR shifts (in ppm) for boronated cyanometallates.

Complex	Abbreviation	11B Shift (ppm)
(TBA)$_4$[Ru(CN-B(C$_6$F$_5$)$_3$)$_6$]	**Ru-II-BCF**	−14.7
(TBA)$_4$[Os(CN-B(C$_6$F$_5$)$_3$)$_6$]	**Os-II-BCF**	−14.4
(PPh$_4$)$_3$[Os(CN-B(C$_6$F$_5$)$_3$)$_6$]	**Os-III-BCF**	−37.6
(TBA)$_4$[Fe(CN-B(C$_6$F$_5$)$_3$)$_6$]^a	**Fe-II-BCF**	−14.6
(TBA)$_3$[Fe(CN-B(C$_6$F$_5$)$_3$)$_6$]	**Fe-III-BCF**	−54.2
(TBA)$_4$[Mn(CN-B(C$_6$F$_5$)$_3$)$_6$]	**Mn-II-BCF**	−60.4
(TBA)$_3$[Mn(CN-B(C$_6$F$_5$)$_3$)$_6$]	**Mn-III-BCF**	−136.1
(TBA)$_4$[Mn(CN-2,4,6-BArF$_9$)$_6$]	**Mn-II-246**	−19.6
(TBA)$_3$[Mn(CN-2,4,6-BArF$_9$)$_6$]	**Mn-III-246**	−113.7

^{a}Reference [53]

Electrochemistry

Voltammetry data for **Fe-II-BCF**, **Ru-II-BCF**, **Os-II-BCF**, **Mn-III-BCF**, **Mn-III-246**, **Cr-III-BCF, Cr-III-CN-BPh$_3$, and Cr-III-NC-BPh$_3$** were collected in MeCN, DCM, or THF with 0.1–0.2 M TBAPF$_6$ as the supporting electrolyte. Potentiostatic electrochemical impedance spectroscopy was used to obtain the cell uncompensated resistance via the linear intercept of a Nyquist plot. >85% of the cell resistance was compensated electronically. This step is important to ensure that peak-to-peak separations in voltammetry at fast scan rates are not artificially increased due to uncompensated resistance, but rather by convolution of heterogeneous electron transfer rates with ones attributable to complex diffusion. Note that heterogeneous electron transfer rate constants depend on solvent and electrode composition.

In addition to solubility and stability requirements, electron transfer reagents for non-aqueous redox flow batteries should have large heterogeneous electron transfer rate constants and peak current ratios near unity.[79,80] The standard rate constant k_0 is related to the dimensionless parameter ψ through **Equation 1**,

$$\psi = \frac{\left(\frac{D_0}{D_R}\right)^{\alpha/2} k_0}{\sqrt{\frac{D_0 \pi v n F}{RT}}} \qquad (1)$$

where D_0 and D_R are diffusion coefficients of the oxidized and reduced electroactive species (cm^2 s^{-1}), v is the scan rate (V s^{-1}), and α is the transfer coefficient for electron transfer. As a result, peak-to-peak separations in cyclic voltammetry inversely correlate with heterogeneous rate constants for outer-sphere electron transfers. Thus, we can assess the relative change in rate constant between parent and boronated species through scan rate-dependent cyclic voltammetry.

Redox couples of boronated cyanometallates are electrochemically reversible, exhibiting comparable or higher electron transfer rate constants than parents, which likely are attributable to lower outer-sphere reorganization energies. Additionally, based on the very slight changes in M-C-N bond lengths accompanying electron transfers, we suggest that inner-sphere reorganization energies are comparable for parent and boronated species. Interestingly, a previous study suggested that self-exchange reactions of metal cyanide complexes are mediated through counterion bridges between cyanides, as their rates decrease by several orders of magnitude upon addition of alkali cation complexing agents.[81] However, high supporting electrolyte concentrations in the Helmholtz plane would disfavor this electron transfer mechanism. **Figures S120-S126** display scan rate dependences and Randles-Sevcik plots for all reversible couples of these complex anions.

Given the anodic formal potentials for some of these species, certain peak current ratios were calculated using an empirical formula that deconvolutes the current at the switching potential from the redox event, **Equation 2**,

$$\frac{i_{p,c}}{i_{p,a}} = \frac{i_{p,c,0}}{i_{p,a,0}} + 0.485 \left(\frac{i_{sp}}{i_{p,a,0}} \right) + 0.086 \qquad (2)$$

where $\frac{i_{p,c}}{i_{p,a}}$ is the corrected peak current ratio, $\frac{i_{p,c,0}}{i_{p,a,0}}$ is the peak current ratio relative to zero current, and $\frac{i_{sp}}{i_{p,a,0}}$ is the ratio of the uncorrected peak anodic current to the current at the switching potential.[82]

Overlays of the voltammetry of all electrochemically reversible species are displayed in **Figure 5**, while formal potentials, peak potentials, ranges of peak-to-peak separations, and peak current ratios are set out in **Table 7**. Formal potentials shift by over 2.1 V for **Fe/Ru/Os-III/II-BCF** complexes. **Fe-III/II-BCF** exhibits the largest shift (2.29 V), which was underestimated in our previous work due to incomplete removal of H_2O coordinated to **Fe-III**.[53] Other inaccurate formal potentials have been reported in the literature for cyanometallates due to the strong binding of H_2O to cyanide.[6,77] **Ru-III/II-BCF** and **Os-III/II-BCF** exhibit nearly identical shifts in formal potentials from those of parents, 2.11 and 2.12 V, respectively. Of note is that **Os-III/II** and **Os-III/II-BCF** exhibit less anodic formal potentials than **Ru-III** and **Ru-III-BCF**, owing in part to greater 5d spin-orbit coupling.[83]
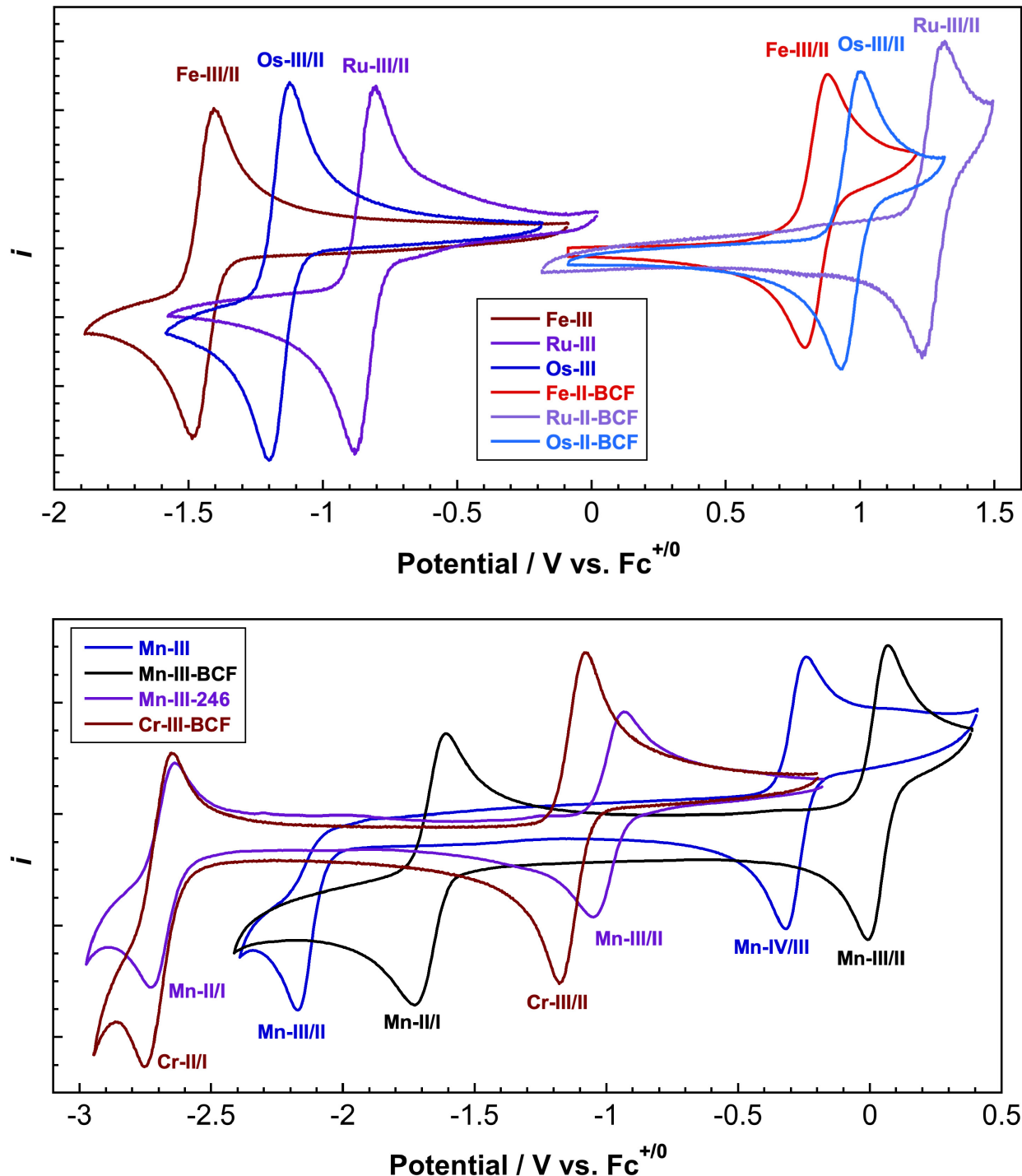
Figure 5. (**Upper**) Overlay of voltammetry of $(TBA)_3[Fe(CN)_6]$ (**Fe-III**), $(Ph_4As)_3[Ru(CN)_6]$ (**Ru-III**), $(Ph_4P)_3[Os(CN)_6]$ (**Os-III**), $(TBA)_4[Fe(CN-B(C_6F_5)_3)_6]$ (**Fe-II-BCF**), $(Ph_4As)_4[Ru(CN-B(C_6F_5)_3)_6]$ (**Ru-II-BCF**), and $(Ph_4P)_4[Os(CN-B(C_6F_5)_3)_6]$ (**Os-II-BCF**) in MeCN. All potentials referenced to $Fc^{+/0}$. (**Lower**) Overlay of voltamme-try of $(TBA)_3[Mn(CN)_6]$ (**Mn-III**) (MeCN), $(TBA)_3[Mn(CN-B(C_6F_5)_3)_6]$ (**Mn-III-BCF**) (MeCN), $(PPN)_3[Mn(CN-B(2,4,6-BArF_9)_3)_6]$ (**Mn-III-246**) (THF), and $(TBA)_3[Cr(CN-B(C_6F_5)_3)_6]$ (**Cr-III-BCF**) (THF). All measurements performed with 0.1–0.2 M $TBAPF_6$ as electrolyte using a 3 mm diameter glassy carbon working electrode, 0.01 M $Ag^{+/0}$ non-aqueous reference electrode, and platinum wire counter electrode.

19

The potential shift for **Cr-III/II-BCF** relative to **Cr-III/II** is 2.08 V. In earlier work, reaction of Cr(II) with potassium cyanide generated alkali salts of **Cr-II**,[74] and subsequent reduction with K/Na metal in liquid ammonia afforded a complex assigned as low-spin Cr(0), $(K/Na)_6[Cr(CN)_6]$.[78] Previous electrochemical studies of **Cr-III** demonstrated that in basic solution with low cyanide concentrations, ligand substitution of CN^- by H_2O occurred through an ECE mechanism, which is unsurprising given the poor backbonding ability of Cr(III).[84]

Table 7. Electrochemical parameters for parent and boronated cyanometallates in MeCN, THF, or DCM solution with 0.1–0.2 M TBAPF$_6$ electrolyte using a glassy carbon working electrode, 0.01 M Ag$^{+/0}$ non-aqueous reference electrode, and platinum wire counter electrode. All formal potentials taken from 100 mV s^{-1} scan rate data. Peak-to-peak separations and peak current ratios taken from 25–2500 mV s^{-1} scan rate data. All formal potentials referenced to Fc$^{+/0}$. Resting state of each compound used given in parentheses.

Redox Couple	Abbreviation	$E_{p,a}$ (V vs. Fc$^{+/0}$)	$E_{p,c}$ (V vs. Fc$^{+/0}$)	E_0' (V vs. Fc$^{+/0}$)	ΔE_p (mV)	$i_{p,a}/i_{p,c}$
$[Cr(CN-B(C_6F_5)_3)_6]^{3/4-a}$	**Cr-III-BCF**	−0.82	−0.92	−0.87	92-174	0.92-1.00
$[Cr(CN-B(C_6F_5)_3)_6]^{4/5-a}$	**Cr-III-BCF**	−2.75	−2.65	−2.70	92-149	0.70-0.76
$[Cr(CN-BPh_3)_6]^{3/4-b}$	**Cr-III-CN-BPh$_3$**	---	−1.60	−1.54^c	---	---
$[Cr(NC-BPh_3)_6]^{3/4-b}$	**Cr-III-NC-BPh$_3$**	---	−1.60	−1.47^c	---	---
$[Mn(CN-B(2,4,6-BArF_9)_3)_6]^{2/3-a}$	**Mn-III-246**	1.17	---	1.13^c	---	---
$[Mn(CN-B(2,4,6-BArF_9)_3)_6]^{3/4-a}$	**Mn-III-246**	−0.93	−1.04	−0.99	85-175	0.92-1.00
$[Mn(CN-B(2,4,6-BArF_9)_3)_6]^{4/5-a}$	**Mn-III-246**	−2.64	−2.73	−2.68	79-118	0.69-0.92
$[Mn(CN-B(C_6F_5)_3)_6]^{2/3-}$	**Mn-III-BCF**	2.07	---	2.00^c	---	---
$[Mn(CN-B(C_6F_5)_3)_6]^{3/4-}$	**Mn-III-BCF**	0.07	−0.01	0.03	79-80	0.99-1.00
$[Mn(CN-B(C_6F_5)_3)_6]^{4/5-}$	**Mn-III-BCF**	−1.61	−1.72	−1.67	95-138	0.90-0.92
$[Fe(CN-B(C_6F_5)_3)_6]^{3/4-}$	**Fe-II-BCF**	0.88	0.79	0.84	74-85	0.88-1.00
$[Ru(CN-B(C_6F_5)_3)_6]^{3/4-}$	**Ru-II-BCF**	1.31	1.23	1.27	85-85	0.79-0.83
$[Os(CN-B(C_6F_5)_3)_6]^{3/4-}$	**Os-II-BCF**	1.00	0.93	0.96	72-83	0.92-1.00
$[Cr(CN)_6]^{3/4-}$	**Cr-III**	---	---	−2.95^d	---	---
$[Cr(CN)_6]^{4/5-}$	**Cr-III**	---	---	−4.78^e	---	---
$[Mn(CN)_6]^{3/4-}$	**Mn-III**	---	−2.18	−2.11^c	---	---
$[Mn(CN)_6]^{2/3-}$	**Mn-III**	−0.24	−0.32	−0.28	79-82	0.93-0.99
$[Fe(CN)_6]^{3/4-}$	**Fe-III**	−1.41	−1.49	−1.45	80-105	0.97-1.00
$[Ru(CN)_6]^{3/4-}$	**Ru-III**	−0.80	−0.88	−0.84	73-93	0.93-1.00
$[Os(CN)_6]^{3/4-}$	**Os-III**	−1.12	−1.20	−1.16	75-107	0.95-1.00
$[Fe(CN)_6]^{3/4-f}$	**Fe-II**	---	---	0.361^f	---	---
$[Ru(CN)_6]^{3/4-f}$	**Ru-II**	---	---	0.926^f	---	---
$[Os(CN)_6]^{3/4-f}$	**Os-II**	---	---	0.636^f	---	---

^{a}Voltammetry acquired in THF solution.
^{b}Voltammetry acquired in DCM solution.
^{c}Taken from the inflection potential of the redox process at 100 mV s^{-1}, which approximates the formal potential. See reference [85].
^{d}Taken from references [86] and [87] (experiments in 1.0 M KCN at a dropping mercury electrode). Derived by using the separation in aqueous formal potentials between $[Fe(CN)_6]^{3-}$ and $[Cr(CN)_6]^{3-}$.
^{e}Taken from the potential separation between **Cr-III/II** and **Cr-II/I** for $(TBA)_3[Cr(CN-B(C_6F_5)_3)_6]$ (**Cr-III-BCF**) in THF solution.
^{f}In neutral, aqueous media vs. NHE. Taken from references [76], [88], and [89].

We observed high chemical stabilities of both **Cr-III-BCF** and **Cr-II-BCF** and reversible **Cr-III/II-BCF** electrochemistry, likely because the sterically blocked metal center disfavors ligand substitution and boronation leads to increased π-backdonation. Due to solubility and stability issues for **Cr-III**, the formal potential shift for **Cr-III-BCF** relative to **Cr-III** in non-aqueous media was calculated using the average potential shift of **Fe/Os/Ru-III** from aqueous to acetonitrile solution ($\mathbf{\Delta}E_{solvent,avg.} = -1.79$ V). We emphasize that the difference between the experimental formal potential for **Cr-III/II-BCF** and that calculated for **Cr-III/II** is fully consistent with the formal potential shifts for other electrochemically reversible species. Based on the experimentally determined **Cr-II/I** formal potential, it is unlikely that a Cr(0) complex was isolated in the earlier work.[78] The shift in $E^{0'}$, estimated from the inflection potential determined from the first derivative of the voltammogram for **Cr-III-CN-BPh₃,** is consistent with the difference between **Fe-III-BCF** and **Fe-III-BPh₃** observed before.[53] The less cathodic formal potential for **Cr-III-NC-BPh₃** vs. **Cr-III-CN-BPh₃** accords with the greater ligand field strength of C-bonded relative to N-bonded cyanide. Additionally, the shift in peak potential as a function of scan rate (41 mV / decade scan rate) for **Cr-III-NC-BPh₃** indicates a kinetically controlled or kinetically intermediate regime for an EC$_i$ mechanism (**Figure S127**).[90] Given the weaker ligand field exerted by a nitrile donor, we suggest that the irreversible chemical reaction involves loss of a [NC-BPh₃]$^-$ ligand upon reduction.

The potential shift of **Mn-III/II-BCF** relative to **Mn-III/II** is 2.14 V. **Mn-III** has been previously characterized in several solvents, exhibiting a linear dependence of formal potential on solvent acceptor number.[23,91] The reported $E^{0'}$(IV/III) = −0.22 V vs. Fc$^{+/0}$ is slightly more anodic than our derived value (−0.28 V vs. Fc$^{+/0}$). This difference could be due to use of tetrabutylammonium (not tetra-ethylammonium) as the counterion. Additionally, the greater reversibility in our case likely stems from use of a glassy carbon rather than a platinum working electrode (cyanides are known to bind to platinum).[92,93] In contrast to **Mn-III**, which exhibited reversible Mn-IV/III and irreversible Mn-III/II redox couples in MeCN solution, we found reversible Mn-III/II and Mn-II/I couples and an irreversible Mn-IV/III couple for **Mn-III-BCF/246.**

Shifts in formal potentials for boronated cyanometallate redox couples correlate roughly with Gutmann-Beckett solvent acceptor numbers, and by extension, borane acceptor numbers (AN). For

Mn-III, the potential shifts anodically by 2.14 V upon coordination of **BCF**, while for **246**, the anodic shift is 1.1 V, or approximately 350 mV for each coordinated **BCF** (AN = 77.15 - 82)[94,95] and 180 mV for each coordinated **246** (AN = 68.5).[96,97] Considering all five **M-III-BCF** species, the potential shift increase tracks with the decrease in average M-C bond length (1.921 Å (**Fe-III-BCF**) < 1.99 Å (**Mn-III-BCF**) < 2.030 Å (**Ru-III-BCF**) < 2.055 Å (**Os-III-BCF**) < 2.065 Å (**Cr-III-BCF**)).

One of the most exciting results is the electrochemical observation of **Mn-I-BCF**, **Mn-I-246**, and **Cr-I-BCF**. Of these three, we were only able to chemically isolate **Mn-I-BCF** (*vide supra*). For **Cr-II/I-BCF**, a peak current ratio much less than one at slower scan rates was observed, likely due to decomposition near the limit of the THF potential window. To our knowledge, this is the first demonstration of these oxidation states in cyanometallate chemistry.

UV-visible-NIR and MCD Spectroscopy
Upon boronation, a descent in symmetry from O_h to D_{3d} occurs, assuming trigonal symmetry for staggered boranes. However, we do not expect degenerate state splittings $T_{1u} \rightarrow A_{2u} + E_u$ and $T_{2u} \rightarrow A_{1u} + E_u$ to perturb LMCT bands as much as lowered orbital energies attributable to borane coordination. Although we anticipated that band profiles similar to those of parent complexes would be systematically shifted in energy due to boronation, we found, using a combination of UV-visible-NIR spectroscopy, spectroelectrochemistry, MCD spectroscopy, and theory, that this is likely not the case. All UV-visible-NIR and MCD spectra were fit employing Gaussian deconvolution techniques with the same number of bands in both cases. Since UV-visible-NIR spectra were acquired at room temperature (**Figures S50-S68**) and MCD spectra were acquired at 5 K (**Figures S72-S87**), FWHM and intensities were allowed to float and band maxima were restricted to within 1000 cm^{-1}. Due to strong $\pi \rightarrow \pi^*$ absorption by phenylboranes, we only analyzed features below 37,000 cm^{-1}.

MCD intensities can be estimated from **Equation 3**,

$$I \propto \left[A \left(\frac{-\partial f(E)}{\partial E} \right) + \left(B_0 + \frac{C_0}{kT} \right) f(E) \right] \quad (3)$$

which includes Faraday *A*-, *B*-, and *C*-terms. The mathematical underpinnings by which paramagnetic species exhibit these different terms are well-documented in the literature.[13,98–100] *C*-term

intensity correlates inversely with temperature, while *A*- and *B*-terms are generally temperature independent. The increase in *C*-term intensity at cryogenic temperatures arises from differential population of spin sublevels in a paramagnetic ground state split by Zeeman interaction with the magnetic field. The similarity in signals observed for **Fe/Ru/Os-III-BCF** led us to conclude that, as with their parents, these spectra are dominated by *C*-term LMCT transitions.[12–17] We note that Upton et al. previously demonstrated that >98% of MCD intensity arises from *C*-terms below 6 K.[16] This conclusion is further supported by examination of room-temperature MCD spectra for all boronated species (**Figures S88-S93**), where there are weak signals that are not observed in the low-temperature spectra. Aside from **Mn-III-BCF**, **Mn-III-246**, and **Cr-II-BCF** (non-Kramers ions), all *C*-term intensities exhibited linear dependences on inverse temperature from 5 to 20 K. Peak maxima, MCD signs, and transition assignments are given in **Table 8** and **Table 9**. MCD behavior is more complex for higher ground-state spin multiplicities, so we restrict detailed analyses to $(t_{2g})^5$ complexes and provide only tentative assignments for $(t_{2g})^4$ and $(t_{2g})^3$ systems.

$(t_{2g})^5$ Complexes

Neglecting spin-orbit coupling interactions, the $(t_{2g})^5$ configuration gives rise to a $^2T_{2g}$ ground state (O_h point group). Excitations to $^2A_{2u}$, ^2E_u, $^2T_{1u}$, and $^2T_{2u}$ states are electric dipole allowed. A basis set of two σ and two π orbitals on each cyanide ligand produces 12 σ molecular orbitals ($2\times a_{1g}$, $2\times e_g$, $2\times t_{1u}$) and 12 π molecular orbitals (t_{1g}, t_{2g}, t_{1u}, t_{2u}) in the parent complexes (**Figure 1**). Considering only one-electron transitions into the dπ t_{2g} vacancy, transitions from the 6 σ_2 orbitals will give $^2A_{1g}$, ^2E_g, and $^2T_{1u}$ excited states. Three analogous states result from one-electron excitation from the 6 σ_1 orbitals. Transitions from the 12 CN π orbitals into the dπ t_{2g} vacancy will produce $^2T_{1g}$, $^2T_{2g}$, $^2T_{1u}$, and $^2T_{2u}$ states. Boronation of the cyanide ligand introduces a second pair of ligand π orbitals arising from interaction of the C≡N π-bonding orbitals with the B-C σ-bonding orbitals. This additional set of π molecular orbitals produces four additional LMCT excited states ($^2T_{1g}$, $^2T_{2g}$, $^2T_{1u}$, and $^2T_{2u}$) (**Figure 6**). Spin-orbit coupling interactions will split the 6-fold degeneracy of ^2T states producing one doubly degenerate and one fourfold-degenerate state ($^2T_{1g/u} \rightarrow E'_{g/u}$, $U'_{g/u}$; $^2T_{2g/u} \rightarrow E''_{g/u}$, $U'_{g/u}$).

In consideration of Group VIII S = ½ complexes, we adopted the assignments proposed by Piepho et al. for hexahalo Ir(IV) anions.[101–103] These complexes exhibit strong LMCT features analogous

to those in the spectra of Group VIII M(III) complexes. The conventions and ordering arise from the assumption of intermediate spin-orbit splitting of the triply degenerate orbital states in the O_h^* double group. We exclude trigonal splitting of the four-fold degenerate $U'_{u/g}$ due to the high symmetries of the primary coordination spheres for these complexes. Excluding spin-orbit coupling, the selection rules based on reduced matrix elements for orbital transitions are given by eqs 4–5 where D_0 is the electric dipole transition strength.

$$\frac{C_0}{D_0}(t_{2g} \rightarrow t_{1u}) = 1 \qquad (4)$$

$$\frac{C_0}{D_0}(t_{2g} \rightarrow t_{2u}) = -1 \qquad (5)$$

We anticipate MCD features attributable to $t_{1u} \rightarrow t_{2g}$ and $t_{2u} \rightarrow t_{2g}$ excitations with approximately equal and opposite differential intensity.[99]
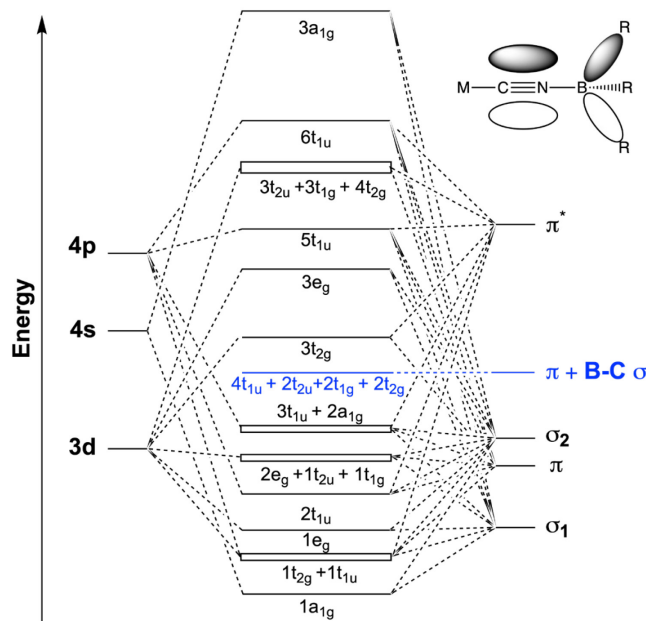
Figure 6. Energy level diagram for cyanometallates including borane-cyanide orbitals.

We first discuss the set **Fe-III-BCF**, **Ru-III-BCF**, and **Os-III-BCF**, where the ground state in O_h^* is E_g'' ($^2T_{2g}$). The orbital numbering and assignments are taken from **Figure 6**. Gaussian deconvolutions of 294 K UV-vis-NIR and 5 K MCD spectra for **Os-III-BCF** are shown in **Figure 7**. The lowest energy features in UV-vis-NIR absorption spectra are broad (FWHM > 3000 cm^{-1}). In room-temperature and low-temperature MCD spectra, bands attributable to overlapping $4t_{1u} \rightarrow$

$3t_{2g}$ [12,800 (Ru), 15,900 (Os), and 17,450 cm^{-1} (Fe) cm^{-1}] and $2t_{2u} \rightarrow 3t_{2g}$ [15,930 (Ru), 18,900 (Os), and 19,280 (Fe) cm^{-1}] LMCT transitions are observed. The charge transfer states, which are unprecedented in homoleptic cyanometallates, likely involve donor levels comprised of linear combinations of borane σ-bonding and cyanide π-bonding orbitals (**Figure 6**). In all three complexes, the differential absorptions for these transitions are unusually small compared to those for higher-energy LMCT transitions, likely due to larger spatial separation of borane-dominated orbitals. Negative MCD intensities for cryogenic samples of Fe, Ru, and Os were not observed, likely due to the greater positive differential intensities for t_{1u} orbital transitions in the region of the negative t_{2u} orbital transition. However, the room-temperature MCD spectra of both Os and Fe display negative MCD intensities in that region, supporting our assignmnets (**Figures S88** and **S89**). In addition to the allowed transitions, we also observe small, positive bands at 9,900 and 12,620 cm^{-1} in the MCD spectra of **Ru-III-BCF** and **Os-III-BCF**. These transitions are unlikely to arise from spin-orbit splitting of the orbital triplets, since the relative energy differences to the $4t_{1u} \rightarrow 3t_{2g}$ transitions are nearly identical for both compounds. This consideration led us to assign these bands to Laporte-forbidden charge transfer transitions ($2t_{2g}$ or $2t_{1g} \rightarrow 3t_{2g}$), which could gain intensity from Herzberg-Teller coupling to the $4t_{1u} \rightarrow 3t_{2g}$ transition. Vibrations of either t_{1u} or t_{2u} symmetry can couple a U'_g/E'_g (t_{1g}), U'_g/E''_g (t_{2g}), or E'_g (a_{1g}) state with the allowed U'_u component of $^2T_{1u}$ to give a positive differential intensity.[101]

We assign the next set of intense features as the $3t_{1u} \rightarrow 3t_{2g}$ orbital transition, dominated by $E''_g \rightarrow U'_u$ (21,140 (Ru), 24,210 (Os), and 24,300 (Fe) cm^{-1}), which is predicted to have much greater C-term intensity relative to $E''_g \rightarrow E'_u$.[101] We also resolved less intense, forbidden charge transfer bands, which we assign to $E''_g \rightarrow E'_g$ ($2a_{1g}$) [21,950 (Ru), 24,940 (Os), and 23,680 (Fe) cm^{-1}] and to $E''_g \rightarrow E'_g/U'_g$ ($1t_{1g}$) [22,420/23,090 (Ru), 25,900 (Os), and 25,190 (Fe) cm^{-1}], all of which gain intensity through the allowed $E''_g \rightarrow U'_u$ ($3t_{1u}$) transition. The last transition to assign in the second charge transfer manifold only appears for **Os-III-BCF** and is due to strong spin-orbit coupling, which splits the $3t_{1u} \rightarrow 3t_{2g}$ components by over 2000 cm^{-1}.[104] Accordingly, we assign the band at 26,950 cm^{-1} to $E''_g \rightarrow E'_u$ ($3t_{1u}$). Being formally forbidden, the transition likely gains intensity through Herzberg-Teller coupling to $E''_g \rightarrow E''_u$ ($1t_{2u}$).

The next manifold of charge transfer states is dominated by $1t_{2u} \rightarrow 3t_{2g}$ orbital transitions, with the most intense negative feature assigned to $E_g'' \rightarrow E_u''$ ($1t_{2u}$) [25,060 (Ru), 28,250 (Os), and 28,740 (Fe) cm^{-1}]. These features are redshifted relative to previously reported values for $1t_{2u} \rightarrow 3t_{2g}$ transitions, with **Fe-III-BCF** exhibiting the greatest redshift, consistent with the nonbonding nature of the t_{2u} cyanide orbitals [and they approximately track with the formal potential of the M(III/II) redox couple, although the energy shift is much smaller than the formal potential shift]. An additional component of the $1t_{2u} \rightarrow 3t_{2g}$ transition, $E_g'' \rightarrow U_u'$ ($1t_{2u}$), is likely present (30,420 (Os), and 29,230 (Fe) cm^{-1}), with shifts in this band consistent with the extent of spin-orbit coupling for each species. We concede that the **Os-III-BCF** band could arise from the forbidden $E_g'' \rightarrow U_g'$ ($2e_g$) LMCT transition, and we suggest that there is a third forbidden LMCT transition, assigned to $E_g'' \rightarrow U_g'$ ($2e_g$) [29,940 (Ru) and 32,000 (Fe) cm^{-1}]. In addition, the third $2t_{1u} \rightarrow 3t_{2g}$ transition, also redshifted from the parent complexes, is assigned to $E_g'' \rightarrow U_u'$ ($2t_{1u}$) [30,680 (Ru), 33,800 (Os), and 34,800 (Fe) cm^{-1}].

Unlike the boronated complexes, the parent $(t_{2g})^5$ complexes do not exhibit any LMCT bands below 20,000 cm^{-1}. Using our boronated spectra, transition assignments of parent $(t_{2g})^5$ M-III spectra have been expanded to account for spin-orbit splitting of LMCT states.[17] For ease of comparison with the boronated complexes, the orbital numberings are taken from **Figure 6**. Based on the shifts in boronated complexes, we assign the first band to $E_g'' \rightarrow U_u'$ ($3t_{1u}$) (20,700 (Ru), 23,900 (Os), and 23,600 (Fe) cm^{-1} and a weaker band to a forbidden transition: $E_g'' \rightarrow E_g'$ ($2a_{1g}$) (21,400 (Ru) and 24,800 (Os) cm^{-1}). All three complexes exhibited features attributable to $E_g'' \rightarrow E_u''$ ($1t_{2u}$) (29,900 (Ru), 32,100 (Os), and 33,700 (Fe) cm^{-1}) and $E_g'' \rightarrow U_u'$ ($2t_{1u}$) (32,100 (Ru), 34,400 (Os), and 37,500 (Fe) cm^{-1}) transitions. Based on previous work,[5] we assign **Fe-III** bands at 31,600 and 35,800 cm^{-1} to $E_g'' \rightarrow E_g'$ ($3t_{2g}$, $^2T_{2g} \rightarrow {}^2T_{1g}$, $^2A_{2g}$ LF transitions) and $E_g'' \rightarrow U_g'$ ($2e_g$); and **Os-III** bands at 25,800 and 30,000 cm^{-1} to $E_g'' \rightarrow E_u'$ ($3t_{1u}$) and $E_g'' \rightarrow E_g'$ ($2e_g$) transitions. An additional band is likely a forbidden LMCT transition, $E_g'' \rightarrow E_g'/U_g'$ ($1t_{1g}$) (27,600 (Ru) and 27,000 (Os) cm^{-1}); alas, the features at 24,200 cm^{-1} (**Os-III**) and 34,100 and 35,200 cm^{-1} (**Ru-III**) remain unassigned.

The **Mn-II-BCF** MCD profile is somewhat different from those of other $(t_{2g})^5$ complexes, likely due to blueshifted LMCT and redshifted MLCT transitions. We assign the two lowest energy bands to $E_g'' \rightarrow U_u'$ $(4t_{1u})$ LMCT and $^2T_{2g} \rightarrow {}^2T_{1g}$, $^2A_{2g}$ LF transitions. The next two transitions could be interchanged between both MLCT and LMCT, though we tentatively assign the band at 32,650 cm^{-1} to $3t_{2g} \rightarrow 5t_{1u}$ and the band at 35,100 cm^{-1} to a $3t_{1u} \rightarrow 3t_{2g}$ transition. MLCT transition energies generally track with the formal potentials for different oxidation states. The lowest-energy MLCT of **Cr-II-BCF** is redshifted by 1.09 eV (8,790 cm^{-1}) from that of **Mn-II-BCF**, while the formal potentials for the two species are separated by 0.9 V, in accord with our assignments.

$(t_{2g})^4$ Complexes

The $(t_{2g})^4$ electronic configuration is complicated by its non-Kramers ($^3T_{1g}$) ground term. First-order spin-orbit coupling splits out a nondegenerate ground state (A_{1g}') with a T_{1g}' state approximately 100 cm^{-1} higher in energy (ground state components E_g' and T_{2g}' lie above A_{1g}' and T_{1g}').[105–109] LMCT bands in hexahalo Os(IV) and Ru(IV) complexes exhibit dominant *A*-terms along with lesser *B*-term intensity. The A_{1g}' / T_{1g}' state separation leads to a much smaller energy denominator for B_0 moments. However, at low temperatures, we anticipate *A*-term intensity from A_{1g}' transitions to dominate. When $kT \geq \Delta$E, we expect the spectrum to be dominated by a combination of *A*-term features due to population of the low-lying T_{1g}' state. Additionally, some *C*-term intensity will arise, though the contribution will be small since all Zeeman sublevels will be populated as kT increases. The spectra of **Mn-III-BCF**, **Mn-III-246**, **Mn-III**, and **Cr-II-BCF** exhibited nonlinear temperature behavior and did not lose much intensity up to 50 K, consistent with expectation. We also note the loss in differential intensity at room temperature, which likely stems from thermal broadening of the LMCT absorption profiles and uniform population of the three T_{1g}' sublevels.

Given the poor resolution of the low-energy region for **Mn-III** and the majority of the **Cr-II-BCF** spectrum, we did not attempt to assign any of the weak bands, which likely correspond to LF transitions for these two species. Like the $(t_{2g})^5$ systems, the lowest-energy charge transfer bands in **Mn-III-BCF** and **Mn-III-246** can be assigned to overlapping $4t_{1u} \rightarrow 3t_{2g}$ (19,740 cm^{-1} (**Mn-III-BCF**) and 22,600 cm^{-1} (**Mn-III-246**)) and $2t_{2u} \rightarrow 3t_{2g}$ (24,870 cm^{-1} (**Mn-III-BCF**) and 26,540 cm^{-1} (**Mn-III-246**)) transitions.

While resolution of components was improved in the next set of orbital triplets, the small spin-orbit coupling constant for Mn(III) and great overlap of bands in these regions did not allow absolute assignments. However, we assign the most intense bands to $A_{1g}' \rightarrow T_{1u}'$ components (which are fully allowed in MCD) of $t_{1u} \rightarrow t_{2g}$ and $t_{2u} \rightarrow t_{2g}$ orbital transitions, along with less intense components. For $3t_{1u} \rightarrow 3t_{2g}$, these occur at 30,140/30,220/30,370 (**Mn-III-246**), 29,980/31,270/31,760 (**Mn-III-BCF**), and 28,880/29,070/29,500/30,220 (**Mn-III**) cm^{-1}. Like the $(t_{2g})^5$ spectra, we also resolved a band attributable to a forbidden LMCT transition [$1t_{1g} \rightarrow 3t_{2g}$, at 33,030 (**Mn-III-246**), 33,140 (**Mn-III-BCF**), and 33,310/34,110 (**Mn-III**) cm^{-1}]. An additional band in the spectrum of **Mn-III-BCF** at 28,820 cm^{-1} remains unassigned. However, we were able to assign higher energy bands to $1t_{2u} \rightarrow 3t_{2g}$ transitions [35,490/35,820 (**Mn-III-246**), 34,540/35,130 (**Mn-III-BCF**), and 35,500 (**Mn-III**) cm^{-1}].

Turning to **Cr-II-BCF** MCD spectra, features at 23,550/24,190 cm^{-1} likely are attributable to $A_{1g}' \rightarrow T_{1u}'$ MLCT transitions, based on the lower formal potential of **Cr-II-BCF** relative to **Mn-III-BCF**. We also assign the band at 36,700 cm^{-1} to the lowest energy $4t_{1u} \rightarrow 3t_{2g}$ LMCT transition.

$(t_{2g})^3$ Complexes

Complexes with $(t_{2g})^3$ ground-state configurations are **Cr-III**, **Cr-III-BCF**, **Cr-III-CN-BPh₃,** and **Cr-III-NC-BPh₃**. The MCD spectra for these species also exhibit C-terms that depend on the degree of zero-field splitting and the geometrical splitting of the U_g' ground state. Owing to small zero-field splitting, with an applied magnetic field of 7 T the $J = -3/2$ sublevel is lowest in energy by about 6 cm^{-1}, leading to preferential absorption of left circularly polarized light. Low temperature MCD spectra of **Cr-III-NC-BPh₃** displayed multiple low-energy, weak **($\Delta\varepsilon_M < 0.2$ M^{-1} cm^{-1} T^{-1})** bands centered at 20,650 cm^{-1} [$^4A_{2g} \rightarrow {}^4T_{2g}$ ($U_g' \rightarrow E_g'$, E_g'', $\frac{3}{2}U_g'$, $\frac{5}{2}U_g'$)].[39]

The spectrum of a boronated Cr(III) complex is quite different from that of **Cr-III**, likely due to overlapping MLCT and LMCT transitions in the parent (MLCT transitions are blueshifted in boronated derivatives). Our assignments are consistent with the MLCT energies of **Mn-II-BCF** and **Mn-III-BCF**. Additionally, the most intense, positive bands for **Cr-III-BCF** and **Cr-III-CN-BPh₃** can be assigned to the lowest energy $4t_{1u} \rightarrow 3t_{2g}$ orbital transitions.

A plot of LMCT band energies vs the formal potentials of all five **M-III-BCF** complexes is linear with a slope near unity **(Figure 8)**, indicating that the transition in question is pure LMCT, with little mixing from other orbitals.
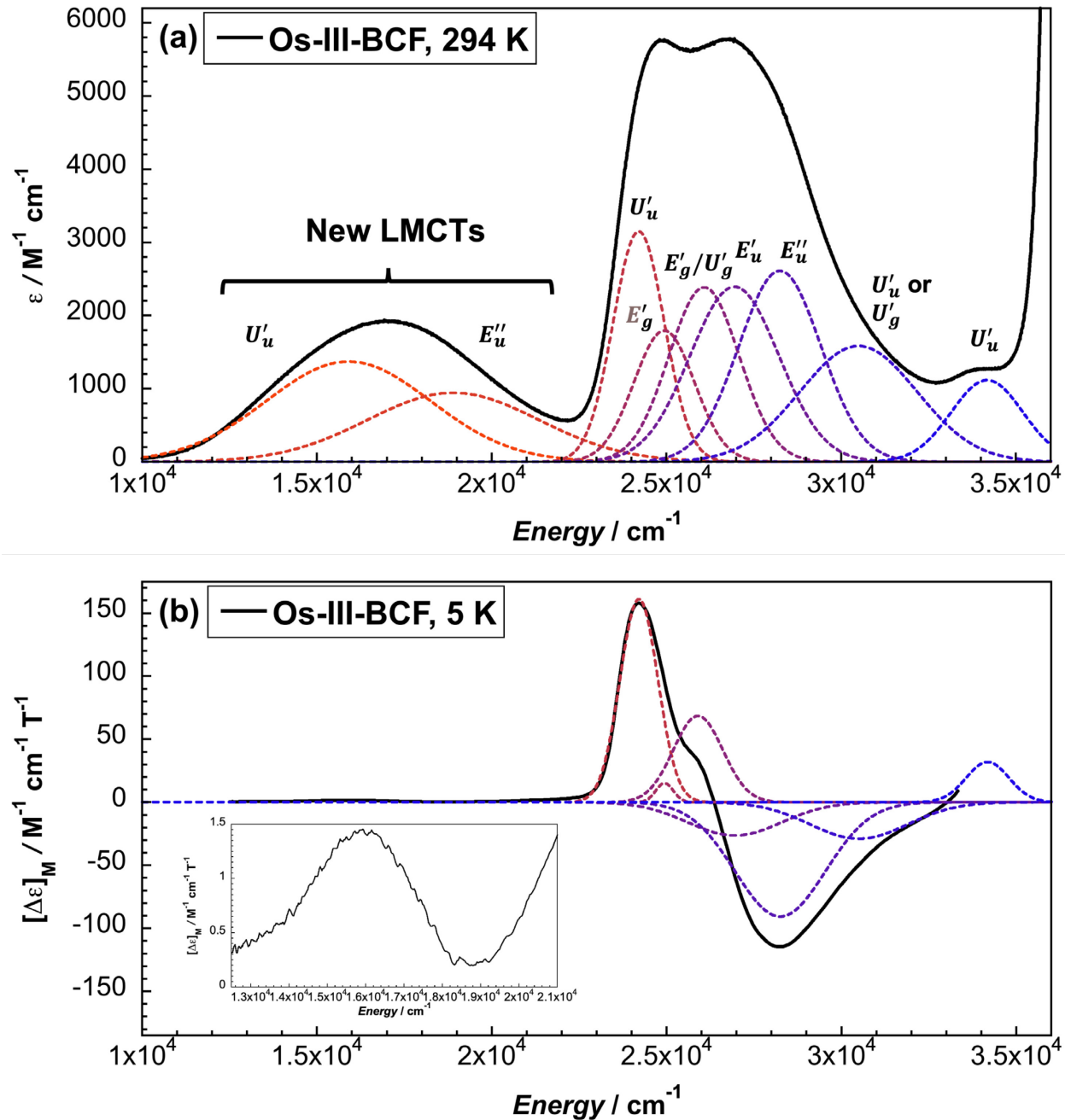

Figure 7. **(a)** Gaussian deconvolution of room-temperature, UV-visible-NIR spectra of (PPh$_4$)$_3$[Os(CN-B(C$_6$F$_5$)$_3$)$_6$] (**Os-III-BCF**) in dichloromethane solution and **(b)** Gaussian deconvolution of the 2 T MCD spectrum of **Os-III-BCF** in a poly(methyl methacrylate) film at 5 K. New LMCTs due to boronation of cyanide are denoted in the UV-vis-NIR spectrum. Due to their low **Δε**/BT values, these low-energy MCD features were not simulated.
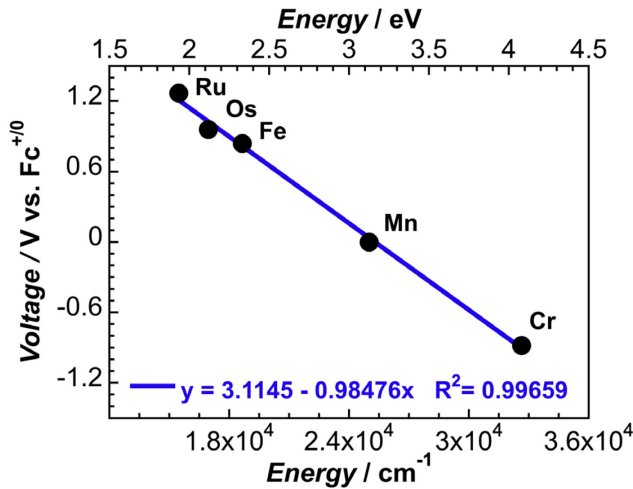
Figure 8. Formal potentials vs the lowest-energy LMCT maximum for **M-III-BCF** complex anions.

Table 8. Absorption band energies, extinction coefficients, and transition assignments for open shell boronated cyanometallates and parent complexes. Spectra of isolated complexes were fit by fixing band maxima with values from resolved peaks observed in MCD (5 K) and UV-vis-NIR (294 K) spectra. The $\pi \rightarrow \pi^*$ borane bands (from ~37,000-40,000 cm^{-1}) are not included in the assignments. Orbital assignments from **Figure 6**.

Complex Anion	Abbreviation	Energy (cm^{-1}) (MCD Sign)	Transition (Donor Orbital)
[Mn(CN-B(2,4,6-C$_6$F$_3$H)$_3$)$_6$]$^{3-}$	**Mn-III-246**	22,600 (−)	$4t_{1u} \rightarrow 3t_{2g}$
		26,540 (+)	$2t_{2u} \rightarrow 3t_{2g}$
		30,140 (−), 30,220 (+), 30,370 (+)	$3t_{1u} \rightarrow 3t_{2g}$
		33,030 (+)	$1t_{1g} \rightarrow 3t_{2g}$
		35,490 (+), 35,820 (−)	$1t_{2u} \rightarrow 3t_{2g}$
[Mn(CN-B(C$_6$F$_5$)$_3$)$_6$]$^{3-}$	**Mn-III-BCF**	19,740 (−)	$4t_{1u} \rightarrow 3t_{2g}$
		24,870 (+)	$2t_{2u} \rightarrow 3t_{2g}$
		28,820 (+)	Forbidden LMCT/LF Transitions
		29,980 (−), 31,270 (+), 31,760 (+)	$3t_{1u} \rightarrow 3t_{2g}$
		33,140 (+)	$1t_{1g} \rightarrow 3t_{2g}$
		34,540 (+), 35,130 (−)	$1t_{2u} \rightarrow 3t_{2g}$
[Mn(CN-B(C$_6$F$_5$)$_3$)$_6$]$^{4-}$	**Mn-II-BCF**	29,100 (+), 30,600 (+)	$E_g'' \rightarrow U_u' (4t_{1u}), E_g'' \rightarrow E_g' (3t_{2g})$
		32,650 (+)	$E_g'' \rightarrow U_u' \left(3t_{2g}\right)$ (MLCT)
		35,100 (+)	$E_g'' \rightarrow U_u' (3t_{1u})$ (LMCT)
[Mn(CN-B(C$_6$F$_5$)$_3$)$_6$]$^{5-}$	**Mn-I-BCF**	27,390	$^1A_{1g} \rightarrow {}^1T_{1u} (2t_{2g})$
[Cr(CN-B(C$_6$F$_5$)$_3$)$_6$]$^{4-}$	**Cr-II-BCF**	23,550 (+), 24,190 (+)	$A_{1g}' \rightarrow T_{1u}' (3t_{2g})$ (MLCT)
		36,700 (−)	$t_{1u} \rightarrow t_{2g} (3t_{1u})$
[Fe(CN-B(C$_6$F$_5$)$_3$)$_6$]$^{3-}$	**Fe-III-BCF**	17,450 (+)	$E_g'' \rightarrow U_u' (4t_{1u})$
		19,280 (−)	$E_g'' \rightarrow E_u'' (2t_{2u})$
		23,680 (+)	$E_g'' \rightarrow E_g' (2a_{1g})$
		24,300 (+)	$E_g'' \rightarrow U_u' (3t_{1u})$
		25,190 (+)	$E_g'' \rightarrow E_g'/U_g' (1t_{1g})$
		28,740 (−)	$E_g'' \rightarrow E_u'' (1t_{2u})$
		29,230 (+)	$E_g'' \rightarrow U_u' (1t_{2u})$
		32,000 (−)	$E_g'' \rightarrow U_g' (2e_g)$
		34,800 (+)	$E_g'' \rightarrow U_u' (2t_{1u})$
[Ru(CN-B(C$_6$F$_5$)$_3$)$_6$]$^{3-}$	**Ru-III-BCF**	9,900 (+)	$E_g'' \rightarrow E_g'/U_g' (2t_{1g})$
		12,800 (+)	$E_g'' \rightarrow U_u' (4t_{1u})$
		15,930 (−)	$E_g'' \rightarrow E_u'' (2t_{2u})$
		21,140 (+)	$E_g'' \rightarrow U_u' (3t_{1u})$

Complex Anion		Energy (cm^{-1}) (MCD Sign)	Transition (Donor Orbital)
		21,950 (+)	$E_g'' \to E_g'\ (2a_{1g})$
		22,420 (+)	$E_g'' \to U_g'\ (1t_{1g})$
		23,090 (+)	$E_g'' \to E_g'\ (1t_{1g})$
		25,060 (−)	$E_u'' \to E_u''\ (1t_{2u})$
		29,940 (−)	$E_g'' \to U_g'\ (2e_g)$
		30,680 (+)	$E_g'' \to U_u'\ (2t_{1u})$
[Os(CN-B(C$_6$F$_5$)$_3$)$_6$]$^{3-}$	**Os-III-BCF**	5,780 (−)	$E_g'' \to U_g'\ (3t_{2g})$
		5,860 (+)	$E_g'' \to U_g'\ (3t_{2g})$
		12,620 (+)	$E_g'' \to E_g'/U_g'\ (2t_{1g})$
		15,900 (+)	$E_g'' \to U_u'\ (4t_{1u})$
		18,900 (−)	$E_g'' \to E_u''\ (2t_{2u})$
		24,210 (+)	$E_g'' \to U_u'\ (3t_{1u})$
		24,940 (+)	$E_g'' \to E_g'\ (2a_{1g})$
		25,900 (+)	$E_g'' \to E_g'/U_g'\ (1t_{1g})$
		26,950 (−)	$E_g'' \to E_u'\ (3t_{1u})$
		28,250 (−)	$E_g'' \to E_u''\ (1t_{2u})$
		30,420 (−)	$E_g'' \to U_u'\ (1t_{2u})$ or $E_g'' \to U_g'\ (2e_g)$
		33,800 (+)	$E_g'' \to U_u'\ (2t_{1u})$

[a]Obtained from spectroelectrochemistry. [b]Spectra collected in DCM solution. [c]Spectra collected in THF solution.

Table 9. Absorption band energies, extinction coefficients, and transition assignments for open shell boronated cyanometallates and parent complexes. Spectra of isolated complexes were fit by fixing band maxima with values from resolved peaks observed in MCD (5 K) and UV-vis-NIR (294 K) spectra. Orbital assignments from **Figure 6**.

Complex Anion	Energy (cm^{-1}) (MCD Sign)	Transition (Donor Orbital)
[Mn(CN)$_6$]$^{3-}$ (Mn-III)	28,880 (−), 29,070 (+), 29,500 (+), 30,220 (−)	$3t_{1u} \to 3t_{2g}$
	33,310 (+), 34,110 (+)	$1t_{1g} \to 3t_{2g}$
	35,500 (−)	$1t_{2u} \to 3t_{2g}$
[Fe(CN)$_6$]$^{3-a}$ (Fe-III)	23,600 (+)	$E_g'' \to U_u', E_u'\ (3t_{1u})$
	31,600 (−)	$E_g'' \to E_g'\ (3t_{2g})$
	33,700 (−)	$E_g'' \to U_u', E_u''\ (1t_{2u})$
	35,800 (−)	$E_g'' \to U_g'\ (2e_g)$
	37,500 (+)	$E_g'' \to U_u'\ (2t_{1u})$
[Ru(CN)$_6$]$^{3-a}$ (Ru-III)	20,700 (+)	$E_g'' \to U_u'\ (3t_{1u})$
	21,400 (+)	$E_g'' \to E_g'\ (2a_{1g})$
	27,600 (−)	$E_g'' \to E_g'/U_g'\ (1t_{1g})$
	29,900 (−)	$E_g'' \to E_u''\ (1t_{2u})$
	32,100 (+)	$E_g'' \to U_u'\ (2t_{1u})$
	34,100 (+)	?
	35,200 (+)	?
[Os(CN)$_6$]$^{3-a}$ (Os-III)	23,900 (+)	$E_g'' \to U_u'\ (3t_{1u})$
	24,200 (+)	?
	24,800 (+)	$E_g'' \to E_g'\ (2a_{1g})$
	25,800 (+)	$E_g'' \to E_u'\ (3t_{1u})$
	27,000 (−)	$E_g'' \to E_g'/U_g'\ (1t_{1g})$
	30,000 (−)	$E_g'' \to E_g'\ (2e_g)$
	32,100 (−)	$E_g'' \to E_u''\ (1t_{2u})$
	34,400 (+)	$E_g'' \to U_u'\ (2t_{1u})$

[a]MCD data taken from reference 17, with updated assignments.

*Spectroelectrochemistry of **Mn-III-BCF** and **Cr-III-BCF***

Owing to the difficulty in isolating pure samples of **Mn-I-BCF** and **Cr-II-BCF**, we turned to spectroelectrochemistry as a reliable means for testing for electrochemical reversibility and determining other properties of the reduced species. Absorption spectra for **Mn-III-BCF** + e$^-$ → **Mn-II-BCF**, **Mn-II-BCF** + e$^-$ → **Mn-I-BCF**, **Cr-III-BCF** + e$^-$ → **Cr-II-BCF** reactions at different applied potentials are shown in **Figure 9**. All reductions were electrochemically reversible, with original spectra regenerated using a reversal potential (**Figure S129**). Gratifyingly, the spectrum generated from one-electron reduction matches that of chemically reduced **Mn-II-BCF** (**Figure S60**). Of interest is the finding from X-ray crystallographic analysis that the ground state of **Mn-I-BCF** is likely low-spin, as confirmed by the growth of an intense absorption band at 27,390 cm^{-1} that is similar to features in Mn(I) arylisocyanide spectra reported by Wenger et al.[110,111] The band in the **Mn-I-BCF** spectrum is likely due to an MLCT ($^1A_{1g}$ → $^1T_{1u}$) transition. Reduction of **Cr-III-BCF** to **Cr-II-BCF** produced a spectrum with an intense band at 28,200 cm^{-1}. The redshift and energy relative to other MLCT transitions in boronated cyanometallates led us to assign this feature to $^3T_{1g}$ → $^3T_{2u}$ MLCT.
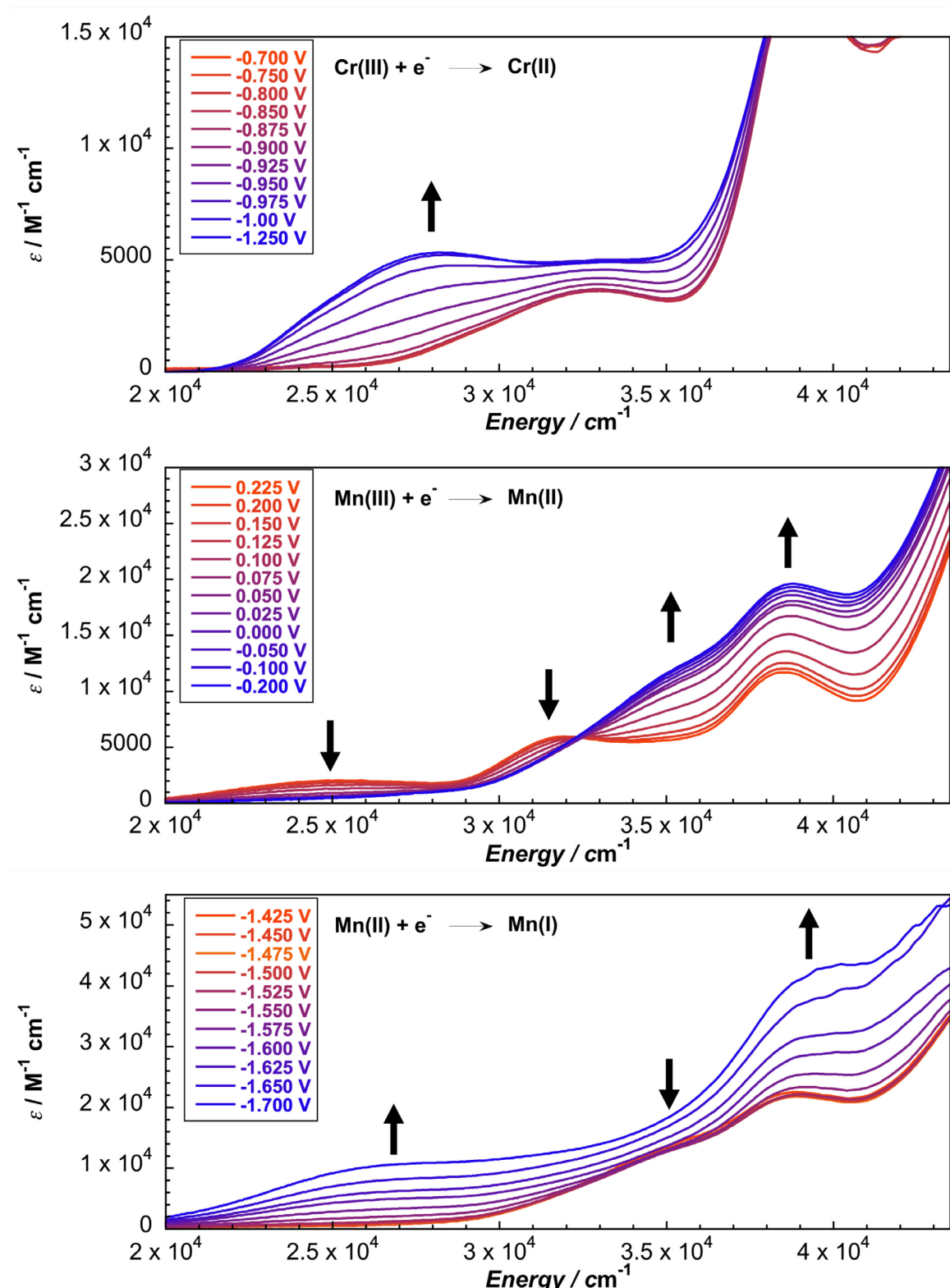
Figure 9. (**Top**) Spectroelectrochemistry of 0.85 mM (TBA)$_3$[Cr(CN-BCF)$_6$] (**Cr-III-BCF**) in THF solution. (**Middle**) and (**Bottom**) Spectroelectrochemistry of 0.28 mM (TBA)$_3$[Mn(CN-BCF)$_6$] (**Mn-III-BCF**) in MeCN solution. Measurements performed with 0.5 M TBAPF$_6$ using a gold working electrode, 0.01 M Ag$^{+/0}$ non-aqueous reference electrode, and platinum wire counter electrode. Electrolysis at each potential was performed for two minutes; all spectra reported were obtained after one minute of electrolysis.

Intraconfigurational (IC) Transitions in Os(III) Complexes

Unique features of **Os-III** electronic structures are IC transitions whose energies fall in the NIR spectral region. For octahedral **Os-III** and **Os-III-BCF**, the $^2T_{2g}$ ground state splits into E_g'' and U_g' (the latter further split into E_g' and E_g'' in D_{3d}) states, which give rise to $E_g'' \rightarrow E_g''$ and $E_g'' \rightarrow E_g'$ IC transitions. NIR spectra were acquired in deuterated dichloromethane to minimize solvent vibrational overtone absorptions (in a control experiment, we found no measurable NIR absorption of 60 mM tetraphenylphosphonium chloride in deuterated DCM solution). Features attributable to $E_g'' \rightarrow E_g''/E_g'$ transitions of **Os-III-BCF** are in **Figure S63**. The NIR MCD spectra of **Os-III-BCF** exhibit positive and negative C-terms, as documented previously for **Os-III** and other Os(III) complexes.[112]

IC transitions of metal complexes can couple to asymmetric vibrational modes to produce false origins by Hertzberg-Teller vibronic coupling. The unresolved fine structure appearing on the high energy side of the **Os-III-BCF** NIR band likely corresponds to vibronic origins in these bulky anions.[113] We observed NIR absorption centered at 8,060 cm^{-1}, which is 2,210 cm^{-1} higher than the IC band center. This energy difference is consistent with vibronic coupling to cyanoborate stretching (2,204 cm^{-1} in **Os-III-BCF**). We also observed $E_g'' \rightarrow E_g''/E_g'$ features and corresponding overtones in low-temperature MCD spectra for **Os-III-BCF**,. Additionally, we measured the NIR absorption spectrum of **Os-III** in DCM solution. The separation of **Os-III** $E_g'' \rightarrow E_g''/E_g'$ bands (224 cm^{-1}) is greater than for **Os-III-BCF** (100 cm^{-1}), see **Figure S63**.

Electronic Structure Calculations

We adopted a descent in symmetry approach to reduce the number of roots that need to be considered in the CASSCF active space required to calculate LMCT transitions for **Fe-III-BCF**, **Ru-III-BCF**, **Os-III-BCF**, and **Mn-II-BCF**. These complexes all have $(t_{2g})^5$ electronic structures, which limit the number of configurations. Exploitation of symmetry has been employed previously in work on homoleptic cyanometallates.[104,114,115] Note that earlier we demonstrated that BCF can be replaced with trihydridoborane (BH$_3$) (a Lewis acid with similar Lewis acidity) to obtain MLCT energies.[54]

All calculations were performed with the Orca 4.2.1 software package.[116] All M-CN-BH$_3$ structures were optimized using the PBE0 functional,[117,118] with the def2-QZVPP basis set on the central metal and the def2-TZVP basis set on all other atoms.[119] The resolution of identity approximation for both Coulomb and HF integrals (RI-JK) was used for all calculations in conjunction with the def2/JK auxiliary basis set.[120] All optimizations employed the conductor-like polarizable continuum model (CPCM) with dichloromethane (ε = 8.93) as the solvent.

After optimization, the structures were reoriented in ChemCraft to retain C$_{2h}$ symmetry (subgroup of D$_{3d}$), which provides a means to separate LF and CT states based on irreducible representations.[121] Each molecule was oriented such that the z-axis was coincident with the principal axis of rotation (C$_2$). Starting orbitals were generated using the PBE0 functional, the def2-QZVPP basis for the central metal atom, and the def2-SVP basis set for all other atoms. The RI-JK approximation, the def2/JK auxiliary basis set, and the CPCM model with DCM were again used. Based on symmetry considerations, an orbital basis of 23 electrons in 17 orbitals was used to obtain roots for t$_{1u}$ and t$_{2u}$ states, with two e$_g$ cyanide σ bonding orbitals, seven CN-BH$_3$ orbitals of a$_u$ symmetry, three t$_{2g}$ π orbitals, two e$_g$ cyanide σ^* antibonding orbitals, and three t$_{2g}$ π^* backbonding orbitals. As a result of overlap of σ-bonding orbitals of borane with orbitals of CN, new bonding/antibonding combinations were generated. **Fe-III-BH$_3$** orbitals are shown in **Figure 10**. The roots for each complex with full active space were selected based on the reduced symmetry and the valence electron configuration: 2 x A$_g$ and 1 x B$_g$ (orbital triplet ground state split in C$_{2h}$ symmetry) and 7 x A$_u$ for the $(a_u)^1(t_{2g})^6$ excited-state configurations. Comparisons of calculated and experimental transition energies are set out in **Table 10**. Trends in relative charge transfer energies are consistent with our experimental assignments and support our conclusions about new LMCT transitions. We correlate our experimental assignments with calculated transitions in **Table 10**. The isosurfaces in **Figure 10** depict the CN-B bonding interactions that contribute to splitting of LMCT states into new energy levels.

Table 10. Calculated and experimental LMCT transition energies for d^5 boronated cyanometallates

Complex	LMCT Energy (CASSCF+NEVPT2) (cm^{-1})	Oscillator Strength	MCD Energy (cm^{-1})
[Mn(CN-BH$_3$)$_6$]$^{4-}$	35,503 (7a$_u$ → t$_{2g}$)	0.0452	29,100/30,600
	41,093 (6a$_u$ → t$_{2g}$)	0.0349	---
	41,359 (5a$_u$ → t$_{2g}$)	0.0360	---
	47,735 (4a$_u$ → t$_{2g}$)	0.000688	35,100
	58,928 (3a$_u$ → t$_{2g}$)	0.00252	---
	59,197 (2a$_u$ → t$_{2g}$)	0.00229	---
	60,581 (1a$_u$ → t$_{2g}$)	0.000848	---
[Fe(CN-BH$_3$)$_6$]$^{3-}$	24,684 (7a$_u$ → t$_{2g}$)	0.0221	17,450
	27,440 (6a$_u$ → t$_{2g}$)	0.0197	19,280
	27,614 (5a$_u$ → t$_{2g}$)	0.0189	---
	37,094 (4a$_u$ → t$_{2g}$)	0.0000225	24,300
	45,991 (3a$_u$ → t$_{2g}$)	0.00210	28,740/29,230
	46,505 (2a$_u$ → t$_{2g}$)	0.00295	34,800
	50,603 (1a$_u$ → t$_{2g}$)	0.0136	---
[Ru(CN-BH$_3$)$_6$]$^{3-}$	18,052 (7a$_u$ → t$_{2g}$)	0.0227	12,800
	19,904 (6a$_u$ → t$_{2g}$)	0.0234	15,930
	19,927 (5a$_u$ → t$_{2g}$)	0.0000916	---
	28,331 (4a$_u$ → t$_{2g}$)	0.0000002	21,140
	39,076 (3a$_u$ → t$_{2g}$)	0.00635	25,060
	39,263 (2a$_u$ → t$_{2g}$)	0.0000171	---
	41,234 (1a$_u$ → t$_{2g}$)	0.00397	30,680
[Os(CN-BH$_3$)$_6$]$^{3-}$	20,122 (7a$_u$ → t$_{2g}$)	0.0443	15,900
	21,994 (6a$_u$ → t$_{2g}$)	0.0427	18,900
	22,344 (5a$_u$ → t$_{2g}$)	0.0407	---
	30,611 (4a$_u$ → t$_{2g}$)	0.000145	24,210
	40,594 (3a$_u$ → t$_{2g}$)	0.00565	28,250
	40,713 (2a$_u$ → t$_{2g}$)	0.00573	---
	42,575 (1a$_u$ → t$_{2g}$)	0.00391	33,800

π* t$_{2g}$ **π* t$_{2g}$**   **π* t$_{2g}$**   **σ* e$_g$**

σ* e$_g$ **π t$_{2g}$**   **π t$_{2g}$**   **π t$_{2g}$**

3t$_{1u}$ **4t$_{2u}$**   **3t$_{2u}$**   **2t$_{1u}$**

2t$_{2u}$ **1t$_{2u}$**   **1t$_{1u}$**   **σ e$_g$**

σ e$_g$
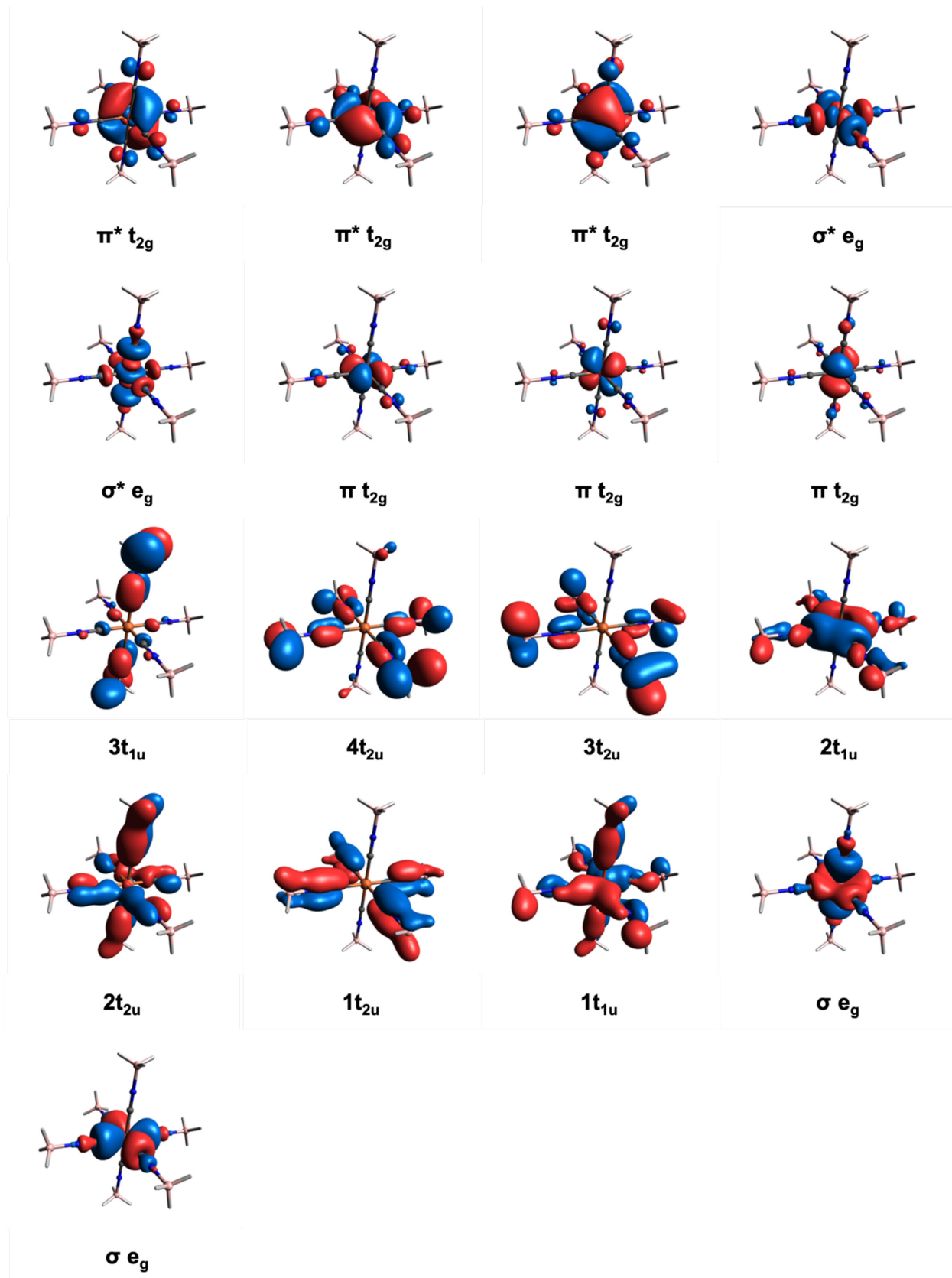
Figure 10. CASSCF+NEVPT2 orbitals for [Fe(CN-BH$_3$)$_6$]$^{3-}$ (**Fe-III-BH$_3$**). Iso-surface set to 0.03.

Luminescence Data

In 1969, photoluminescence at 22,650 cm^{-1} was observed upon excitation of a single crystal of K$_4$[Ru(CN)$_6$] (77 K) by a mercury arc lamp.[122] The luminescence lifetime was about 32 ms and was assigned to a spin-forbidden LF (^{3}T$_{1g} \rightarrow \,^1$A$_{1g}$) transition. For the boronated complex, **Ru-II-BCF**, emission was not observed upon excitation red of 27,000 cm^{-1}, in accord with expectation (the ^{3}T$_{1g}$ state is blue shifted relative to that of the parent anion). Note, however, that 37,600 cm^{-1} excitation produced a broad luminescence profile centered at 24,930 cm^{-1} (14.8 K), corresponding to a 2,300 cm^{-1} blue shift relative to that of the parent (**Figure 11**). The magnitude of this shift accords with that for the ^{1}A$_{1g} \rightarrow \,^1$T$_{1g}$ transition in the **Fe-II-BCF** absorption spectrum (2,400 cm^{-1} based on Gaussian fitting; the ^{1}A$_{1g} \rightarrow \,^1$T$_{1g}$ maximum is 29,060 cm^{-1}).[53]

K$_4$[Os(CN)$_6$] luminesces at 20,900 cm^{-1} (77 K) upon excitation from a mercury arc lamp.[122] Analogous to **Ru-II-BCF**, **Os-II-BCF** ^{3}T$_{1g} \rightarrow \,^1$A$_{1g}$ emission (24,860 cm^{-1} at 13 K) is blue shifted relative to the parent (**Figure 11**).

Surprisingly, **Ru-III** is luminescent, a rare example of radiative decay from an LMCT excited state.[123] However, LMCT emission is absent in both **Fe-III** and **Os-III**.[123,124] We were hopeful that redshifts in the lowest LMCT bands of **Ru-III-BCF** and **Os-III-BCF** would be accompanied by NIR luminescence. However, we were unable to observe emission from either complex, even at low temperature (13.0 K). We acknowledge the possibility that self-quenching could occur for the powdered samples that were tested.

The ^{2}E$_g \rightarrow \,^4$A$_{2g}$ phosphorescence of **Cr-III** has been investigated extensively, as have excited-state substitution reactions.[87,125–127] For comparison, we measured low-temperature luminescence spectra for **Cr-III-BCF**, **Cr-III-CN-BPh$_3$**, and **Cr-III-NC-BPh$_3$**. Biexponential fits were used to determine average decay times at 77 K after 28,200 cm^{-1} excitation (**Table 11)**. An increase in average decay time was observed upon boronation, likely owing to a decrease in nonradiative decay pathways attributable to interactions with solvent molecules.
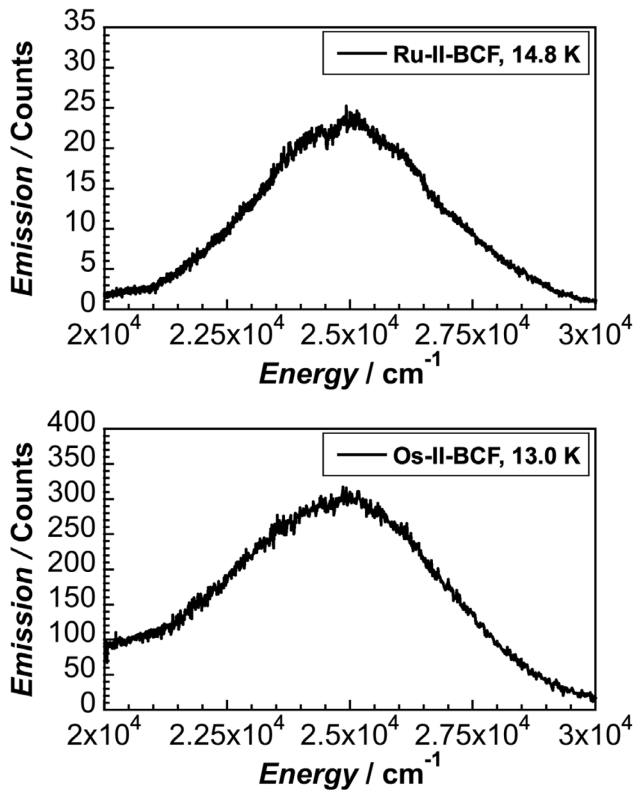
Figure 11. Powder emission spectra of (upper) (TBA)$_4$[Ru(CN-B(C$_6$F$_5$)$_3$)$_6$] (**Ru-II-BCF**) (14.8 K) and (lower) (TBA)$_4$[Os(CN-B(C$_6$F$_5$)$_3$)$_6$] (**Os-II-BCF**) (13.0 K).

Table 11. Emission maxima (λ_{max}) and average decay lifetimes (τ_{avg}) for Cr(III) complexes.

Species	Solvent	τ_{avg} (Temperature)	λ_{max} (Temperature)
(TBA)$_3$[Cr(CN-B(C$_6$F$_5$)$_3$)$_6$] (**Cr-III-BCF**)	2-MeTHF	46.7 ms (77 K)	12,040 cm^{-1} (23.7 K)
(TBA)$_3$[Cr(CN-BPh$_3$)$_6$] (**Cr-III-CN-BPh$_3$**)	2-MeTHF	10.5 ms (77 K)	11,940 cm^{-1} (17.9 K)
(TBA)$_3$[Cr(NC-BPh$_3$)$_6$] (**Cr-III-NC-BPh$_3$**)	2-MeTHF	9.9 ms (77 K)	13,700 cm^{-1} (24.9 K)
(TBA)$_3$[Cr(CN)$_6$] (**Cr-III**)[a]	H$_2$O/Ethylene Glycol/MeOH	3.95 ms (77 K)	12,450 cm^{-1} (77.0 K)

[a]Reference [128]

EPR Spectroscopy

We collected EPR spectroscopic data to confirm the Cr(III) coordination structures of **Cr-III-CN-BPh$_3$** and **Cr-III-NC-BPh$_3$**. We utilized pulse EPR techniques, namely Q-band (34 GHz) and X-band (9.7 GHz) hyperfine sublevel correlation (HYSCORE) spectroscopy, as they provide information about ligand hyperfine couplings that are often too small to be resolved in an inhomogenously broadened CW-EPR spectrum.

The Q-band electron spin echo (ESE) detected field-swept EPR (ESE-EPR) spectra and Q-band HYSCORE spectra of **Cr-III-CN-BPh$_3$** and **Cr-III-NC-BPh$_3$** are shown in **Figure 12**. All complexes exhibited extremely narrow isotropic spectra with g_{iso} = 1.9925, 1.9924, and 1.9825 for **Cr-**

III-BCF, **Cr-III-CN-BPh₃** and **Cr-III-NC-BPh₃**, respectively. An upper bound of $\Delta g \leq 0.0006$ can be estimated by variation of the g-anisotropy in the ESE-EPR simulations. All three complexes exhibited extremely small zero-field splittings (ZFS), with simulations of the Q-band ESE-EPR spectra indicating axial ZFS values of D = 70, 65, and 25 MHz for **Cr-III-BCF**, **Cr-III-CN-BPh₃** and **Cr-III-NC-BPh₃**, and relatively low ZFS rhombicities of E/D = 0.07, 0.08, and 0.12. The HYSCORE spectra for these complexes confirmed the assigned coordination in each BCF complex, as couplings to ¹⁴N are far greater ($A(^{14}N)$ = [7.2, 7.2, 6.2] MHz) in the N-bound isomer than in the C-bound complex ($A(^{14}N)$ = [−1.2, −1.2, 2.0] MHz). In both complexes, very weak hyperfine coupling to ¹¹B was detected ($A(^{11}B)$ = 0.5-0.7 MHz), consistent with the larger distance of boron than C or N to the metal center. The Q-band HYSCORE spectrum of **Cr-III-BCF** is nearly identical with that of **Cr-III-CN-BPh₃**, with simulations using identical ¹⁴N and ¹¹B coupling parameters to that of **Cr-III-BCF** providing an equivalent fit to the **Cr-III-CN-BPh₃** spectrum (**Figure S135**).

We also recorded X-band CW-EPR spectra for d⁵ boronated cyanometallates in frozen THF or DCM solutions (**Figure 13**). For **Fe-III**, g = [2.35, 2.10, 0.91].[129] The g-tensor for **Fe-III-BCF** exhibited enhanced rhombicity relative to the parent, with g = [2.47, 1.92, 1.35], likely owing to greater inner sphere distortions in the sterically crowded anion. In contrast, g = [1.863, 1.790, 1.690] for **Os-III-BCF** which is much closer to an isotropic pattern than parent g values [1.79, 1.79, 1.21].[6] The decreased anisotropy is consistent with the smaller tetragonal distortion calculated from NIR spectra. In general, many first-order electronic effects will contribute to changes in the observed g tensor. We believe the nephelauxetic effect is at play in tempering deviations below the free-electron value for boronated complexes. We also believe that simultaneous addition of new LMCTs and shifting of ligand field transitions upon boronation have a significant effect, moving values both closer and further away from g = 2.0023. Finally, **Mn-III-BCF**, **Mn-II-BCF**, **Mn-III-246**, and **Mn-II-246** all exhibited very small or no signal in both perpendicular and parallel mode CW-EPR at 5 K.
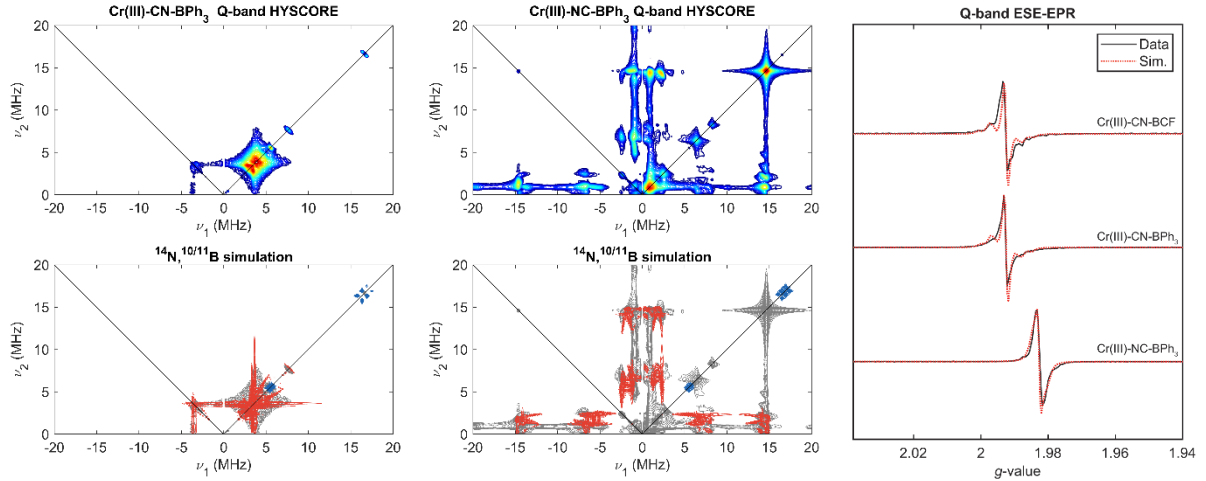
Figure 12. (Left) Pseudomodulated Q-band electron spin-echo (ESE) detected EPR (ESE-EPR) spectrum (black) of frozen solutions of 2.5 mM Cr(III) complexes in frozen glasses of 1:1 propionitrile/2-MeTHF with simulations overlaid in red. Simulation parameters: all complexes are S = 3/2; (TBA)$_3$[Cr(CN-B(C$_6$F$_5$)$_3$)$_6$] (**Cr-III-BCF**): g_{iso} = 1.9925, D = 70 MHz, E/D = .07; (Ph$_4$As)$_3$[Cr(CN-BPh$_3$)$_6$] (**Cr-III-CN-BPh$_3$**): g_{iso} = 1.9924, D = 65 MHz, E/D = .08; (Ph$_4$As)$_3$[Cr(NC-BPh$_3$)$_6$] (**Cr-III-NC-BPh$_3$**): g_{iso} = 1.9825, D = 25 MHz, E/D = .12. **(Middle)** Q-band HYSCORE spectrum of **Cr-III-CN-BPh$_3$** with simulations of ^{14}N couplings overlaid in red and $^{10/11}$B overlaid in blue underneath. **Cr-III-CN-BPh$_3$** simulation parameters: $A(^{14}$N) = [−1.2, −1.2, 2.0] MHz, $e^2qQ/h(^{14}$N$_a$) = 1.8 MHz, $\eta(^{14}$N$_a$) = 0; $A(^{11}$B) = [0.5, 0.5, 0.7] MHz, $e^2qQ/h(^{11}$B) ≤ 0.3 MHz, $\eta(^{11}$B) = 0. **(Right)** Q-band HYSCORE spectrum of **Cr-III-NC-BPh$_3$** with simulations of ^{14}N couplings overlaid in red and $^{10/11}$B overlaid in blue underneath. **Cr-III-NC-BPh$_3$** simulation parameters: $A(^{14}$N) = [7.2, 7.2, 6.2] MHz, $e^2qQ/h(^{14}$N) = 2.4 MHz, $\eta(^{14}$N) = 0; $A(^{11}$B) = [0.4, 0.4, 0.5] MHz, $e^2qQ/h(^{11}$B) ≤ 0.3 MHz, $\eta(^{11}$B) = 0.
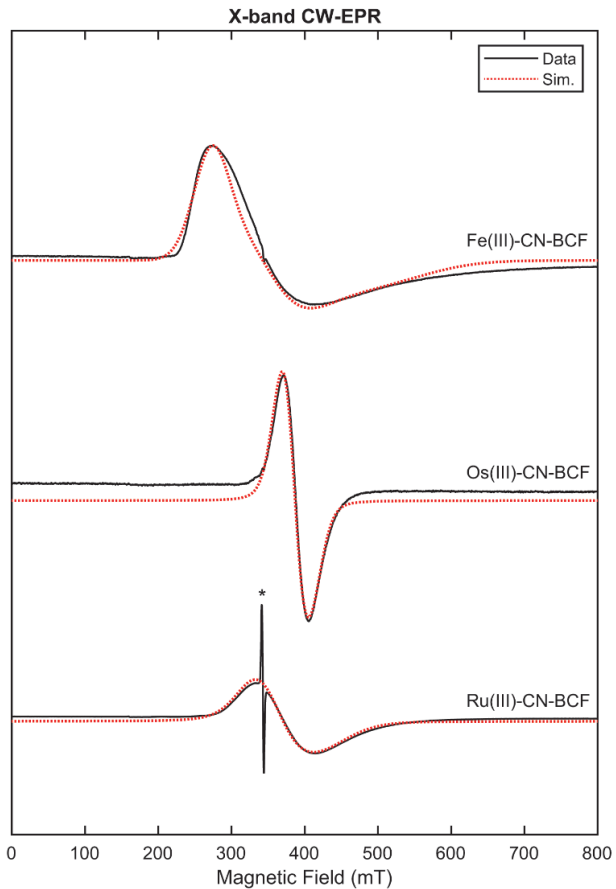
Figure 13. X-band CW-EPR spectra (black) of frozen solutions of $(TBA)_3[Fe(CN-B(C_6F_5)_3)_6]$ (**Fe-III-BCF**), $(Ph_4P)_3[Os(CN-B(C_6F_5)_3)_6]$ (**Os-III-BCF**), and $(Ph_4As)_3[Ru(CN-B(C_6F_5)_3)_6]$ (**Ru-III-BCF**) complexes in frozen solutions of 2Me-THF (Fe) and DCM (Ru and Os) with simulations overlaid in red. Acquisition parameters: temperature = 5 K; MW freq. = 9.638 GHz (Fe), 9.636 GHz (Ru), 9.636 GHz (Os); MW power = 2 mW (Fe and Os), 8 mW (Ru); modulation amplitude = 0.8 mT; conversion time = 81.92 ms. Simulation parameters: Fe: g = [2.47, 1.92, 1.35]; isotropic linewidth = 15 mT; H-strain = [1600, 1500, 1500] MHz; g-strain = [0.2, 0.45, 0.4] MHz; Os: g = [1.863, 1.790, 1.690]; isotropic linewidth = 20 mT; g-strain = [0.2, 0.12, 0.15] MHz. Ru: g = [1.985, 1.896, 1.616]; isotropic linewidth = 60 mT; g-strain = [0.19, 0.35, 0.3] MHz.

Concluding Remarks

We have presented a comprehensive investigation of the fundamental ground- and excited-state electronic structures of boronated cyanometallates. Notably, boronation makes low oxidation states such as Mn(I) and Cr(II) accessible in cyanide complexes. Of special interest is that new ligand-to-metal charge transfer transitions in paramagnetic cyanometallates arise from CN π and B-C σ bonding interactions. These transitions dramatically change the absorption properties of the complexes, as evidenced by their UV-vis-NIR and MCD profiles. Simultaneous UV-vis-NIR and MCD deconvolution allowed us to assign most charge transfer transitions with confidence. Our analysis, coupled with results from theoretical calculations, provides new insights into the effects

of boronation on covalency. Non-aqueous voltammetry of all complexes revealed large anodic shifts in formal potentials upon boronation, expanding on previous findings.[52] Our electrochemical observations provide a practical framework for researchers to predict ground- and excited-state electronic properties of homoleptic and heteroleptic cyanometallates as a function of Lewis acidity. Importantly, the complexes reported here are excellent candidates for advanced spectroscopic investigations that could shed new light on charge distributions in cyanometallates.

ASSOCIATED CONTENT

Supporting Information

Synthetic details, computational calculation parameters, additional UV-vis-NIR, MCD, electrochemistry, and EPR data and parameters. This supporting information is available free of charge on the ACS Publications website.

AUTHOR INFORMATION

Corresponding Authors

Brendon J. McNicholas − Division of Chemistry and Chemical Engineering, California Institute of Technology, Pasadena, California 91125, United States; orcid.org/0000-0002-3654-681X; Email: bmcnicho@caltech.edu

Harry B. Gray − Division of Chemistry and Chemical Engineering, California Institute of Technology, Pasadena, California 91125, United States; orcid.org/0000-0002-7937-7876; Email: hbgray@caltech.edu

Emmanuelle Despagnet-Ayoub − Department of Chemistry, Occidental College, 1600 Campus Road, Los Angeles, California 90041, United States of America; orcid.org/0000-0002-9013-7574; Email: edespagnetay@oxy.edu

Authors

Cherish Nie − Division of Chemistry and Chemical Engineering, California Institute of Technology, Pasadena, California 91125, United States; orcid.org/0000-0002-3758-9950

Anex Jose − Department of Chemistry, Stanford University, 333 Campus Drive, Stanford, California 94305, United States; orcid.org/0000-0002-4924-7886

Paul H. Oyala − Division of Chemistry and Chemical Engineering, California Institute of Technology, Pasadena, California 91125, United States; orcid.org/0000-0002-8761-4667

Michael K. Takase − Division of Chemistry and Chemical Engineering, California Institute of Technology, Pasadena, California 91125, United States

Lawrence M. Henling − Division of Chemistry and Chemical Engineering, California Institute of Technology, Pasadena, California 91125, United States

Alexandra T. Barth − Division of Chemistry and Chemical Engineering, California Institute of Technology, Pasadena, California 91125, United States; orcid.org/0000-0002-1813-4029

Alessio Amaolo − Division of Chemistry and Chemical Engineering, California Institute of Technology, Pasadena, California 91125, United States; orcid.org/0000-0002-9973-6872

Ryan G. Hadt − Division of Chemistry and Chemical Engineering, California Institute of Technology, Pasadena, California 91125, United States; orcid.org/0000-0001-6026-1358

Edward I. Solomon − Department of Chemistry, Stanford University, 333 Campus Drive, Stanford, California 94305, United States; orcid.org/0000-0003-0291-3199

Jay R. Winkler − Beckman Institute, California Institute of Technology, Pasadena, California 91125, United States; orcid.org/0000-0002-4453-9716

Author Contributions

All authors have given approval to the final version of the manuscript.

REFERENCES

1. Macquer, P.-J. Éxamen Chymique de Bleu de Prusse. *Mémoires de l'Académie royale des Sciences* **1752**, 60–77.
2. Gmelin, L. Ueber Ein Besonderes Cyaneisenkalium, and Über Eine Neue Reihe von Blausauren Eisensalzen. *Journal Für Chemie Und Physik* **1822**, *34*, 325–346.
3. Chadwick, B. M.; Sharpe, A. G. Transition Metal Cyanides and their Complexes. *Adv. Inorg. Chem. Radiochem.* **1966**, *8*, 83-176. DOI: 10.1016/S0065-2792(08)60201-0.
4. Chadwick, B. M.; Sharpe, A. G. The Relative Sizes of the Cr(III), Mn(III), Fe(III), and Co(III) Ions in Low-Spin Octahedral Complexes. *J Chem Soc A* **1966**, No. 0, 1390–1391. https://doi.org/10.1039/J19660001390.
5. Alexander, J. J.; Gray, H. B. Electronic Structures of Hexacyanometalate Complexes. *J. Am. Chem. Soc.* **1968**, *90* (16), 4260–4271. https://doi.org/10.1021/ja01018a013.
6. Albores, P.; Slep, L. D.; Baraldo, L. M.; Baggio, R.; Garland, M. T.; Rentschler, E. Crystal Structure and Electronic and Magnetic Properties of Hexacyanoosmate(III). *Inorg. Chem.* **2006**, *45* (6), 2361–2363. https://doi.org/10.1021/ic0516818.
7. Krause, R. A.; Violette, C. An Improved Synthesis of Potassium Hexacyanoruthenate(II). *Inorganica Chim. Acta* **1986**, *113* (2), 161–162. https://doi.org/10.1016/S0020-1693(00)82239-2.
8. Bendix, J.; Steenberg, P.; Søtofte, I. Isolation and Molecular Structure of Hexacyanoruthenate(III). *Inorg. Chem.* **2003**, *42* (15), 4510–4512. https://doi.org/10.1021/ic034287n.
9. Alexander, J. J.; Gray, H. B. Molecular Orbital Theory for Metal Complexes: Ferrocyanide and Cobalticyanide Ions. *Coord. Chem. Rev.* **1967**, *2* (1), 15–28. https://doi.org/10.1016/S0010-8545(00)80191-5.
10. Gray, H. B.; Beach, N. A. The Electronic Structures of Octahedral Metal Complexes. I. Metal Hexacarbonyls and Hexacyanides. *J. Am. Chem. Soc.* **1963**, *85* (19), 2922–2927. https://doi.org/10.1021/ja00902a014.
11. Samuel, R. Absorptionsspektren Komplexer Salze Der Metalle Fe, Co, Ni, Pd, Pt. *Z. Für Phys.* **1931**, *70* (1), 43–73. https://doi.org/10.1007/BF01391030.
12. Stephens, P. J. The Faraday Rotation of Allowed Transitions: Charge-Transfer Transitions in $K_3Fe(CN)_6$. *Inorg. Chem.* **1965**, *4* (12), 1690–1692. https://doi.org/10.1021/ic50034a003.
13. Stephens, P. J. Magnetic Circular Dichroism. *Annu. Rev. Phys. Chem.* **1974**, *25* (1), 201–232. https://doi.org/10.1146/annurev.pc.25.100174.001221.
14. Gale, R.; McCaffery, A. J. Bonding Studies from Charge-Transfer Absorption and Magnetic Circular Dichroism Spectra. Part II. The Complex Hexacyanoferrate(III) and Pentacyanoferrate(III) Complexes of C_{4v}, Symmetry. *J Chem Soc Dalton Trans* **1973**, No. 13, 1344–1351. https://doi.org/10.1039/DT9730001344.
15. Schatz, P. N.; McCaffery, A. J.; Suëtaka, W.; Henning, G. N.; Ritchie, A. B.; Stephens, P. J. Faraday Effect of Charge-Transfer Transitions in $Fe(CN)_6^{3-}$, MnO_4^-, and CrO_4^{2-}. *J. Chem. Phys.* **1966**, *45* (2), 722–734. https://doi.org/10.1063/1.1727633.
16. Upton, A. H. P.; Williamson, B. E. Magnetic Circular Dichroism and Absorption Spectra of Hexacyanoferrate(III) in a Poly(Vinyl Alcohol) Film. *J. Phys. Chem.* **1994**, *98* (1), 71–76. https://doi.org/10.1021/j100052a013.

17. Kang, H. W.; Moran, G.; Krausz, E. Magnetic Circular Dichroism Spectroscopy of the Hexacyano Complexes of Ru(III) and Os(III). *Inorganica Chim. Acta* **1996**, *249* (2), 231–235. https://doi.org/10.1016/0020-1693(96)05090-6.

18. Verdaguer, M.; Girolami, G. S. Magnetic Prussian Blue Analogs. In *Magnetism: Molecules to Materials V*; John Wiley & Sons, Ltd, 2004; pp 283–346. https://doi.org/10.1002/3527604383.ch9.

19. Buschmann, W. E.; Miller, J. S. Magnetic Ordering and Spin-Glass Behavior in First-Row Transition Metal Hexacyanomanganate(IV) Prussian Blue Analogues. *Inorg. Chem.* **2000**, *39* (11), 2411–2421. https://doi.org/10.1021/ic991308y.

20. Zhang, S.-L.; Zhao, X.-H.; Wang, X.-Y. Syntheses, Structures, and Magnetic Properties of Three New Cyano-Bridged Complexes Based on the $[Mn(CN)_6]^{3-}$ Building Block. *Dalton Trans* **2015**, *44* (34), 15189–15197. https://doi.org/10.1039/C5DT00038F.

21. Nelson, K. J.; Daniels, M. C.; Reiff, W. M.; Troff, S. A.; Miller, J. S. $[Cr^{III}(NCMe)_6]^{3+}$ - a Labile Cr^{III} Source Enabling Formation of $Cr[M(CN)_6]$ (M = V, Cr, Mn, Fe) Prussian Blue-Type Magnetic Materials. *Inorg. Chem.* **2007**, *46* (24), 10093–10107. https://doi.org/10.1021/ic7008489.

22. Gutmann, V.; Gritzner, G.; Danksagmuller, K. Solvent Effects on the Redox Potential of Hexacyanoferrate(III)-Hexacyanoferrate(II). *Inorganica Chim. Acta* **1976**, *17*, 81–86. https://doi.org/10.1016/S0020-1693(00)81961-1.

23. Gritzner, G.; Danksagmüller, K.; Gutmann, V. Solvent Effects on the Redox Potentials of Tetraethylammonium Hexacyanomanganate(III) and Hexacyanoferrate(III). *J. Electroanal. Chem. Interfacial Electrochem.* **1978**, *90* (2), 203–210. https://doi.org/10.1016/S0022-0728(78)80054-0.

24. Gritzner, G.; Danksagmüller, K.; Gutmann, V. Outer-Sphere Coordination Effects on the Redox Behaviour of the $Fe(CN)_6^{3-}/Fe(CN)_6^{4-}$ Couple in Non-Aqueous Solvents. *J. Electroanal. Chem. Interfacial Electrochem.* **1976**, *72* (2), 177–185. https://doi.org/10.1016/S0022-0728(76)80166-0.

25. Gutmann, V. Solvent Effects on the Reactivities of Organometallic Compounds. *Coord. Chem. Rev.* **1976**, *18* (2), 225–255. https://doi.org/10.1016/S0010-8545(00)82045-7.

26. Gutmann, V. *The Donor Acceptor Approach to Molecular Interactions*; Plenum Press: New York, 1978.

27. Mayer, U.; Gutmann, V.; Gerger, W. The Acceptor Number — A Quantitative Empirical Parameter for the Electrophilic Properties of Solvents. *Monatshefte Für Chem. Chem. Mon.* **1975**, *106* (6), 1235–1257. https://doi.org/10.1007/BF00913599.

28. Shriver, D. F. The Ambient Nature of Cyanide. In *Structure And Bonding*; Springer Berlin Heidelberg: Berlin, Heidelberg, 1966; pp 32–58.

29. Woodcock, C.; Shriver, D. F. Electrochemistry and Spectroscopy of Dicyanobis(Phenanthroline)Iron, Tetracarbonyltetrakis(Cyclopentadienyl)Tetrairon and Dicarbonylcyano(Cyclopentadienyl)Iron in an Acidic Molten Salt. *Inorg. Chem.* **1986**, *25* (13), 2137–2142. https://doi.org/10.1021/ic00233a008.

30. Indelli, M. Teresa.; Bignozzi, C. Alberto.; Marconi, Anna.; Scandola, Franco. Ruthenium(II) 2,2'-Bipyridine Complexes Containing Methyl Isocyanide Ligands. Extreme Effects of Nonchromophoric Ligands on Excited-State Properties. *J. Am. Chem. Soc.* **1988**, *110* (22), 7381–7386. https://doi.org/10.1021/ja00230a018.

31. Winkler, J. R.; Creutz, C.; Sutin, N. Solvent Tuning of the Excited-State Properties of (2,2'-Bipyridine)Tetracyanoferrate(II): Direct Observation of a Metal-to-Ligand Charge-

Transfer Excited State of Iron(II). *J. Am. Chem. Soc.* **1987**, *109* (11), 3470–3471. https://doi.org/10.1021/ja00245a053.

32. Nichols, A. W.; Machan, C. W. Secondary-Sphere Effects in Molecular Electrocatalytic CO_2 Reduction. *Front. Chem.* **2019**, *7*. https://doi.org/10.3389/fchem.2019.00397.

33. Schmeier, T. J.; Dobereiner, G. E.; Crabtree, R. H.; Hazari, N. Secondary Coordination Sphere Interactions Facilitate the Insertion Step in an Iridium(III) CO_2 Reduction Catalyst. *J. Am. Chem. Soc.* **2011**, *133* (24), 9274–9277. https://doi.org/10.1021/ja2035514.

34. Khosrowabadi Kotyk, J. F.; Hanna, C. M.; Combs, R. L.; Ziller, J. W.; Yang, J. Y. Intramolecular Hydrogen-Bonding in a Cobalt Aqua Complex and Electrochemical Water Oxidation Activity. *Chem Sci* **2018**, *9* (10), 2750–2755. https://doi.org/10.1039/C7SC04960A.

35. Shriver, D. F. Bridge Adducts-the Interaction of BF_3 with Transition Metal Cyanide Complexes. *J. Am. Chem. Soc.* **1962**, *84* (23), 4610–4611. https://doi.org/10.1021/ja00882a061.

36. Shriver, D. F. Preparation and Structures of Metal Cyanide-Lewis Acid Bridge Compounds. *J. Am. Chem. Soc.* **1963**, *85* (10), 1405–1408. https://doi.org/10.1021/ja00893a011.

37. Shriver, D. F.; Posner, J. Bridge Addition Compounds. III. The Influence of Boron-Containing Lewis Acids on Electronic Spectra, Vibrational Spectra, and Oxidation Potentials of Some Iron-Cynanide Complexes. *J. Am. Chem. Soc.* **1966**, *88* (8), 1672–1677. https://doi.org/10.1021/ja00960a018.

38. Zhou, J.; Lancaster, S. J.; Walker, D. A.; Beck, S.; Thornton-Pett, M.; Bochmann, M. Synthesis, Structures, and Reactivity of Weakly Coordinating Anions with Delocalized Borate Structure: The Assessment of Anion Effects in Metallocene Polymerization Catalysts. *J. Am. Chem. Soc.* **2001**, *123* (2), 223–237. https://doi.org/10.1021/ja002820h.

39. Schelter, E. J.; Shatruk, M.; Heintz, R. A.; Galán-Mascarós, J. R.; Dunbar, K. R. Unexpected Conversion of a Hexacyanometallate to a Homoleptic Nitrile Complex with Triphenylborane Substituents. *Chem Commun* **2005**, No. 11, 1417–1419. https://doi.org/10.1039/B414262D.

40. Chu, W.-K.; Ko, C.-C.; Chan, K.-C.; Yiu, S.-M.; Wong, F.-L.; Lee, C.-S.; Roy, V. A. L. A Simple Design for Strongly Emissive Sky-Blue Phosphorescent Neutral Rhenium Complexes: Synthesis, Photophysics, and Electroluminescent Devices. *Chem. Mater.* **2014**, *26* (8), 2544–2550. https://doi.org/10.1021/cm4038654.

41. Chu, W.-K.; Yiu, S.-M.; Ko, C.-C. Neutral Luminescent Bis(Bipyridyl) Osmium(II) Complexes with Improved Phosphorescent Properties. *Organometallics* **2014**, *33* (23), 6771–6777. https://doi.org/10.1021/om500630c.

42. Chan, K.-C.; Chu, W.-K.; Yiu, S.-M.; Ko, C.-C. Synthesis, Characterization, Photophysics and Electrochemical Study of Luminescent Iridium(III) Complexes with Isocyanoborate Ligands. *Dalton Trans* **2015**, *44* (34), 15135–15144. https://doi.org/10.1039/C5DT00904A.

43. Chan, K.; Cheng, S.; Lo, L. T.; Yiu, S.; Ko, C. Luminescent Charge-Neutral Copper(I) Phenanthroline Complexes with Isocyanoborate Ligand. *Eur. J. Inorg. Chem.* **2018**, *2018* (7), 897–903. https://doi.org/10.1002/ejic.201701205.

44. Xiao, Y.; Chu, W.-K.; Ng, C.-O.; Cheng, S.-C.; Tse, M.-K.; Yiu, S.-M.; Ko, C.-C. Design and Synthesis of Luminescent Bis(Isocyanoborato) Rhenate(I) Complexes as a Selective Sensor for Cyanide Anion. *Organometallics* **2020**, *39* (11), 2135–2141. https://doi.org/10.1021/acs.organomet.0c00204.

45. Schmid, L.; Kerzig, C.; Prescimone, A.; Wenger, O. S. Photostable Ruthenium(II) Isocyanoborato Luminophores and Their Use in Energy Transfer and Photoredox Catalysis. *JACS Au* **2021**, *1* (6), 819–832. https://doi.org/10.1021/jacsau.1c00137.

46. Schmid, L.; Glaser, F.; Schaer, R.; Wenger, O. S. High Triplet Energy Iridium(III) Isocyanoborato Complex for Photochemical Upconversion, Photoredox and Energy Transfer Catalysis. *J. Am. Chem. Soc.* **2022**, *144* (2), 963–976. https://doi.org/10.1021/jacs.1c11667.

47. Schmid, L.; Chábera, P.; Rüter, I.; Prescimone, A.; Meyer, F.; Yartsev, A.; Persson, P.; Wenger, O. S. Borylation in the Second Coordination Sphere of Fe^{II} Cyanido Complexes and Its Impact on Their Electronic Structures and Excited-State Dynamics. *Inorg. Chem.* **2022**. https://doi.org/10.1021/acs.inorgchem.2c01667.

48. Ge, J.; Fan, L.; Rao, A. M.; Zhou, J.; Lu, B. Surface-Substituted Prussian Blue Analogue Cathode for Sustainable Potassium-Ion Batteries. *Nat. Sustain.* **2022**, *5* (3), 225–234. https://doi.org/10.1038/s41893-021-00810-7.

49. Huang, B.; Shao, Y.; Liu, Y.; Lu, Z.; Lu, X.; Liao, S. Improving Potassium-Ion Batteries by Optimizing the Composition of Prussian Blue Cathode. *ACS Appl. Energy Mater.* **2019**, *2* (9), 6528–6535. https://doi.org/10.1021/acsaem.9b01097.

50. Wang, W.; Gang, Y.; Hu, Z.; Yan, Z.; Li, W.; Li, Y.; Gu, Q.-F.; Wang, Z.; Chou, S.-L.; Liu, H.-K.; Dou, S.-X. Reversible Structural Evolution of Sodium-Rich Rhombohedral Prussian Blue for Sodium-Ion Batteries. *Nat. Commun.* **2020**, *11* (1), 980. https://doi.org/10.1038/s41467-020-14444-4.

51. Lin, K.; Chen, Q.; Gerhardt, M. R.; Tong, L.; Kim, S. B.; Eisenach, L.; Valle, A. W.; Hardee, D.; Gordon, R. G.; Aziz, M. J.; Marshak, M. P. Alkaline Quinone Flow Battery. *Science* **2015**, *349* (6255), 1529–1532. https://doi.org/10.1126/science.aab3033.

52. Luo, J.; Hu, B.; Debruler, C.; Bi, Y.; Zhao, Y.; Yuan, B.; Hu, M.; Wu, W.; Liu, T. L. Unprecedented Capacity and Stability of Ammonium Ferrocyanide Catholyte in PH Neutral Aqueous Redox Flow Batteries. *Joule* **2019**, *3* (1), 149–163. https://doi.org/10.1016/j.joule.2018.10.010.

53. McNicholas, B. J.; Grubbs, R. H.; Winkler, J. R.; Gray, H. B.; Despagnet-Ayoub, E. Tuning the Formal Potential of Ferrocyanide over a 2.1 V Range. *Chem Sci* **2019**, *10* (12), 3623–3626. https://doi.org/10.1039/C8SC04972F.

54. Ngo, D. X.; Del Ciello, S. A.; Barth, A. T.; Hadt, R. G.; Grubbs, R. H.; Gray, H. B.; McNicholas, B. J. Electronic Structures, Spectroscopy, and Electrochemistry of $[M(Diimine)(CN-BR_3)_4]^{2-}$ (M = Fe, Ru; R = Ph, C_6F_5) Complexes. *Inorg. Chem.* **2020**, *59* (14), 9594–9604. https://doi.org/10.1021/acs.inorgchem.0c00632.

55. Ngo, D. X.; Ciello, S. A. D.; McNicholas, B. J.; Sanders, B. C.; Fajardo, J.; Gray, H. B.; Winkler, J. R. Cyano-Ambivalence: Spectroscopy and Photophysics of $[Ru(Diimine)(CN-BR_3)_4]^{2-}$ Complexes. *Polyhedron* **2020**, *188*, 114692. https://doi.org/10.1016/j.poly.2020.114692.

56. Graham, M. J.; Zadrozny, J. M.; Shiddiq, M.; Anderson, J. S.; Fataftah, M. S.; Hill, S.; Freedman, D. E. Influence of Electronic Spin and Spin–Orbit Coupling on Decoherence in Mononuclear Transition Metal Complexes. *J. Am. Chem. Soc.* **2014**, *136* (21), 7623–7626. https://doi.org/10.1021/ja5037397.

57. Curtis, J. C.; Meyer, T. J. Outer-Sphere Charge Transfer in Mixed-Metal Ion Pairs. *Inorg. Chem.* **1982**, *21* (4), 1562–1571. https://doi.org/10.1021/ic00134a059.

58. Ginsberg, A. P.; Koubek, E. Hydrogen Bonding in Ferrocyanic, Ruthenocyanic, and Osmocyanic Acids. *Inorg. Chem.* **1965**, *4* (8), 1186–1194. https://doi.org/10.1021/ic50030a022.

59. Eller, S.; Fischer, R. D. Convenient Synthesis of Tris(Tetrabutylammonium) Hexacyanoruthenate(III): First Access to a Pure Salt of a Hexacyanoruthenate(III) Anion and to a Coordination Polymer Thereof. *Inorg. Chem.* **1990**, *29* (6), 1289–1290. https://doi.org/10.1021/ic00331a032.

60. Samsonenko, D. G.; Vostrikova, K. E. Effective Preparation of a Variety of Ruthenium and Osmium Cyanides: Valuable Precursors for Molecular Nanomagnets. *Eur. J. Inorg. Chem.* **2016**, *2016* (9), 1369–1375. https://doi.org/10.1002/ejic.201501354.

61. Schläfer, H. L.; Wagener, H.; Wasgestian, F.; Herzog, G.; Ludi, A. Elektronenspektren von Hexacyanochromaten. *Berichte Bunsenges. Für Phys. Chem.* **1971**, *75* (9), 878–883. DOI: 10.1002/bbpc.19710750904.

62. Das, B.; Carlin, R.; Osteryoung, R. A. The Ferro/Ferricyanide Couple in an Aluminum Chloride-1-Methyl-3-Ethylimidazolium Chloride Ambient-Temperature Molten Salt. *Inorg. Chem.* **1989**, *28* (3), 421–426. https://doi.org/10.1021/ic00302a011.

63. Hodge, S. A.; Buckley, D. J.; Yau, H. C.; Skipper, N. T.; Howard, C. A.; Shaffer, M. S. P. Chemical Routes to Discharging Graphenides. *Nanoscale* **2017**, *9* (9), 3150—3158. https://doi.org/10.1039/c6nr10004j.

64. Avendano, C.; Karadas, F.; Hilfiger, M.; Shatruk, M.; Dunbar, K. R. Cyanide Lability and Linkage Isomerism of Hexacyanochromate(III) Induced by the Co(II) Ion. *Inorg. Chem.* **2010**, *49* (2), 583–594. https://doi.org/10.1021/ic901681e.

65. Figgis, B. N.; Forsyth, J. B.; Reynolds, P. A. Spin Density of the Hexacyanochromate(III) Ion Measured by Polarized Neutron Diffraction. *Inorg. Chem.* **1987**, *26* (1), 101–105. https://doi.org/10.1021/ic00248a021.

66. Geier, J.; Willner, H.; Lehmann, C. W.; Aubke, F. Formation of Hexacarbonylmanganese(I) Salts, $[Mn(CO)_6]^+X^-$, in Anhydrous HF. *Inorg. Chem.* **2007**, *46* (17), 7210–7214. https://doi.org/10.1021/ic700798z.

67. Nelson, K. J.; Giles, I. D.; Shum, W. W.; Arif, A. M.; Miller, J. S. The Myth of Cyanide Always Being a Strong-Field Ligand: Synthesis and Structural Characterization of Homoleptic S=2 Pentacyanochromate(II), $[Cr^{II}(CN)_5]^{3-}$, and Nonacyanodichromate(II), $[Cr_2(CN)_9]^{5-}$. *Angew. Chem. Int. Ed.* **2005**, *44* (20), 3129–3132. https://doi.org/10.1002/anie.200462763.

68. Nakamura, M. Is Cyanide Really a Strong-Field Ligand? *Angew. Chem. Int. Ed.* **2009**, *48* (15), 2638–2640. https://doi.org/10.1002/anie.200805446.

69. Lord, R. L.; Baik, M.-H. Why Does Cyanide Pretend to Be a Weak Field Ligand in $[Cr(CN)_5]^{3-}$? *Inorg. Chem.* **2008**, *47* (10), 4413–4420. https://doi.org/10.1021/ic8000653.

70. Gentil, L. A.; Navaza, A.; Olabe, J. A.; Rigotti, G. E. The Crystal and Molecular Structure of Sodium Hexacyanoosmate(II) Decahydrate and Related Hexacyanometalate Complexes. *Inorganica Chim. Acta* **1991**, *179* (1), 89–96. https://doi.org/10.1016/S0020-1693(00)85378-5.

71. Ouahab, L.; Bouherour, S.; Auffredic, J.-P.; Grandjean, D. Tris-(Tetraethylammonium) Hexacyanoferrate (III): Stability of Its Hydrates and X-Ray Structure of the Pentahydrate. *J. Solid State Chem.* **1989**, *82* (1), 139–145. https://doi.org/10.1016/0022-4596(89)90233-8.

72. Buschmann, W. E.; Liable-Sands, L.; Rheingold, A. L.; Miller, J. S. Structure and Physical Properties of Hexacyanomanganate(III), $[Mn^{III}(CN)_6]^{3-}$. *Inorganica Chim. Acta* **1999**, *284* (2), 175–179. https://doi.org/10.1016/S0020-1693(98)00284-9.

73. Alborés, P.; Slep, L. D.; Weyhermüller, T.; Rentschler, E.; Baraldo, L. M. Exchange Coupling across the Cyanide Bridge: Structural and DFT Interpretation of the Magnetic Properties of a Binuclear Chromium(III) Complex. *Dalton Trans* **2006**, No. 7, 948–954. https://doi.org/10.1039/B508386A.

74. Ljungstr, E.; Magniez, G. J.; Chaminade, J.-P.; Pouchard, M.; Hagenmuller, P.; Andresen, A. F. The Crystal Structure of Sodium Hexacyanochromate(II). *Acta Chem. Scand.* **1977**, *8*, 104-108. DOI: 10.3891/ACTA.CHEM.SCAND.31A-0104.

75. Cioran, A. M.; Teixidor, F.; Viñas, C. The Effect of a Paramagnetic Metal Ion within a Molecule: Comparison of the Structurally Identical Paramagnetic $[3,3-Fe(1,2-C_2B_9H_{11})_2]^-$ with the Diamagnetic $[3,3-Co(1,2-C_2B_9H_{11})_2]^-$ Sandwich Complexes. *Dalton Trans* **2015**, *44* (6), 2809–2818. https://doi.org/10.1039/C4DT03418J.

76. Opekar, F.; Beran, P. Electrochemical Oxidation of $K_4Os(CN)_6$ on a Platinum Electrode. *J. Electroanal. Chem. Interfacial Electrochem.* **1976**, *71* (1), 120–124. https://doi.org/10.1016/S0022-0728(76)80296-3.

77. E. Buschmann, W.; Vazquez, C.; D. Ward, M.; C. Jones, N.; S. Miller, J. Structure and Physical Properties of Hexacyanomanganate(Iv), $[Mn^{IV}(CN)_6]^{2-}$. *Chem Commun* **1997**, No. 4, 409–410. https://doi.org/10.1039/A606979G.

78. Eaton, J. P.; Nicholls, D. The Complex Cyanides of Chromium(II) and Chromium(0). *Transit. Met. Chem.* **1981**, *6* (4), 203–206. https://doi.org/10.1007/BF00618223.

79. Weber, A. Z.; Mench, M. M.; Meyers, J. P.; Ross, P. N.; Gostick, J. T.; Liu, Q. Redox Flow Batteries: A Review. *J. Appl. Electrochem.* **2011**, *41* (10), 1137. https://doi.org/10.1007/s10800-011-0348-2.

80. Soloveichik, G. L. Flow Batteries: Current Status and Trends. *Chem. Rev.* **2015**, *115* (20), 11533–11558. https://doi.org/10.1021/cr500720t.

81. Zahl, A.; van Eldik, R.; Swaddle, T. W. Cation-Independent Electron Transfer between Ferricyanide and Ferrocyanide Ions in Aqueous Solution. *Inorg. Chem.* **2002**, *41* (4), 757–764. https://doi.org/10.1021/ic010957i.

82. Nicholson, R. S. Semiempirical Procedure for Measuring with Stationary Electrode Polarography Rates of Chemical Reactions Involving the Product of Electron Transfer. *Anal. Chem.* **1966**, *38* (10), 1406–1406. https://doi.org/10.1021/ac60242a030.

83. Srnec, M.; Chalupský, J.; Fojta, M.; Zendlová, L.; Havran, L.; Hocek, M.; Kývala, M.; Rulíšek, L. Effect of Spin−Orbit Coupling on Reduction Potentials of Octahedral Ruthenium(II/III) and Osmium(II/III) Complexes. *J. Am. Chem. Soc.* **2008**, *130* (33), 10947–10954. https://doi.org/10.1021/ja800616s.

84. Feldberg, S. W.; Jeftic, L. Nuances of the ECE Mechanism. IV. Theory of Cyclic Voltammetry and Chronoamperometry and the Electrochemical Reduction of Hexacyanochromate(III). *J. Phys. Chem.* **1972**, *76* (17), 2439–2446. https://doi.org/10.1021/j100661a017.

85. Espinoza, E. M.; Clark, J. A.; Soliman, J.; Derr, J. B.; Morales, M.; Vullev, V. I. Practical Aspects of Cyclic Voltammetry: How to Estimate Reduction Potentials When Irreversibility Prevails. *J. Electrochem. Soc.* **2019**, *166* (5), H3175–H3187. https://doi.org/10.1149/2.0241905jes.

86. Kane-Maguire, N. A. P.; Guckert, J. A.; O'Neill, P. J. Electrogenerated Chemiluminescence of Hexacyanochromate(III) and Tris(2,2'-Bipyridine)Chromium(III) in Aprotic Solvents. *Inorg. Chem.* **1987**, *26* (14), 2340–2342. https://doi.org/10.1021/ic00261a036.

87. Hume, D. N.; Kolthoff, I. M. The Oxidation Potential of the Chromocyanide—Chromicyanide Couple and the Polarography of the Chromium Cyanide Complexes1. *J. Am. Chem. Soc.* **1943**, *65* (10), 1897–1901. https://doi.org/10.1021/ja01250a030.

88. Murray, R. C.; Rock, P. A. The Determination of the Ferrocyanide—Ferricyanide Standard Electrode Potential at 25°C in Cells without Liquid Junction Using Cation-Sensitive Glass Electrodes. *Electrochimica Acta* **1968**, *13* (4), 969–975. https://doi.org/10.1016/0013-4686(68)85028-5.

89. Crumbliss, A. L.; Hill, H. A. O.; Page, D. J. The Electrochemistry of Hexacyanoruthenate at Carbon Electrodes and the Use of Ruthenium Compounds as Mediators in the Glucose/Glucose Oxidase System. *J. Electroanal. Chem. Interfacial Electrochem.* **1986**, *206* (1), 327–331. https://doi.org/10.1016/0022-0728(86)90280-9.

90. Bard, A. J.; Faulkner, L. R. *Electrochemical Methods: Fundamentals and Applications*, 2nd ed.; Wiley: New York, 2001.

91. Gritzner, G. Solvent Effects on Redox Potentials: Studies in N-Methylformamide. *J. Electroanal. Chem. Interfacial Electrochem.* **1983**, *144* (1), 259–277. https://doi.org/10.1016/S0022-0728(83)80160-0.

92. Weusten, S. J. C.; Groot, M. T. de; Schaaf, J. van der. A Comparative Study of the Stability of Hexachloroiridate and Hexacyanoferrate in Electrochemical Mass Transfer Measurements. *J. Electroanal. Chem.* **2020**, *878*, 114512. https://doi.org/10.1016/j.jelechem.2020.114512.

93. Petrovic, S. Cyclic Voltammetry of Hexachloroiridate(IV): An Alternative to the Electrochemical Study of the Ferricyanide Ion. *Chem. Educ.* **2000**, *5* (5), 231–235. https://doi.org/10.1007/s00897000416a.

94. Sivaev, I. B.; Bregadze, V. I. Lewis Acidity of Boron Compounds. *Coord. Chem. Rev.* **2014**, *270–271*, 75–88. https://doi.org/10.1016/j.ccr.2013.10.017.

95. Beckett, M. A.; Brassington, D. S.; Coles, S. J.; Hursthouse, M. B. Lewis Acidity of Tris(Pentafluorophenyl)Borane: Crystal and Molecular Structure of $B(C_6F_5)_3 \cdot OPEt_3$. *Inorg. Chem. Commun.* **2000**, *3* (10), 530–533. https://doi.org/10.1016/S1387-7003(00)00129-5.

96. Blagg, R. J.; Simmons, T. R.; Hatton, G. R.; Courtney, J. M.; Bennett, E. L.; Lawrence, E. J.; Wildgoose, G. G. Novel B(Ar′)$_2$(Ar″) Hetero-Tri(Aryl)Boranes: A Systematic Study of Lewis Acidity. *Dalton Trans* **2016**, *45* (14), 6032–6043. https://doi.org/10.1039/C5DT03854E.

97. Soltani, Y.; Adams, S. J.; Börger, J.; Wilkins, L. C.; Newman, P. D.; Pope, S. J. A.; Melen, R. L. Synthesis and Photophysical Properties of Imine Borane Adducts towards Vapochromic Materials. *Dalton Trans* **2018**, *47* (36), 12656–12660. https://doi.org/10.1039/C8DT03019G.

98. Piepho, S. B.; Schatz, P. N. *Group Theory in Spectroscopy With Applications to Magnetic Circular Dichroism*; Wiley: New York, 1983.

99. Theoretical Framework: Definition of MCD Terms. In *A Practical Guide to Magnetic Circular Dichroism Spectroscopy*; John Wiley & Sons, Ltd, 2007; pp 14–35. https://doi.org/10.1002/9780470139233.ch3.

100.   Solomon, E. I.; Neidig, M. L.; Schenk, G. 2.26 - Magnetic Circular Dichroism of Paramagnetic Species. In *Comprehensive Coordination Chemistry II*; McCleverty, J. A., Meyer, T. J., Eds.; Pergamon: Oxford, 2003; pp 339–349. https://doi.org/10.1016/B0-08-043748-6/01216-0.

101.   Piepho, S. B.; Lester, T. E.; McCaffery, A. J.; Dickinson, J. R.; Schatz, P. N. The Electronic Absorption and Magnetic Circular Dichroism Spectra of $IrBr_6^{2-}$ in Several Host Crystals. *Mol. Phys.* **1970**, *19* (6), 781–802. https://doi.org/10.1080/00268977000101821.

102.   Dickinson, J. R.; Piepho, S. B.; Spencer, J. A.; Schatz, P. N. High Resolution Magnetic Circular Dichroism and Absorption Spectra of $Cs_2ZrBr_6:Ir^{4+}$. *J. Chem. Phys.* **1972**, *56* (6), 2668–2677. https://doi.org/10.1063/1.1677595.

103.   McCaffery, A. J.; Schatz, P. N.; Lester, T. E. Magnetic Circular Dichroism of $IrCl_6^{2-}$ in Crystalline $(CH_3NH_3)_2SnCl_6$. *J. Chem. Phys.* **1969**, *50* (1), 379–385. https://doi.org/10.1063/1.1670807.

104.   Van den Heuvel, W.; Hendrickx, M. F. A.; Ceulemans, A. A CASPT2 Study of the Electronic Spectrum of Hexacyanoosmate(III). *Inorg. Chem.* **2007**, *46* (19), 8032–8037. https://doi.org/10.1021/ic7004612.

105.   Collingwood, J. C.; Schwartz, R. W.; Schatz, P. N.; Patterson, H. H. Magnetic Circular Dichroism and Absorption Spectra of $Cs_2ZrCl_6:Mo^{4+}$. *Mol. Phys.* **1974**, *27* (5), 1291–1317. https://doi.org/10.1080/00268977400101121.

106.   Solomon, E. I.; Lever, A. B. P. *Inorganic Electronic Structure and Spectroscopy, Volume I*, 1st ed.; Wiley, 2006.

107.   Griffith. *The Theory of Transition-Metal Ions*; Cambridge University Press, 1961.

108.   Cooke, A. H.; Duffus, H. J. The Magnetic Susceptibility of Potassium Manganicyanide. *Proc. Phys. Soc. Sect. A* **1955**, *68* (1), 32–34. https://doi.org/10.1088/0370-1298/68/1/305.

109.   Ghosh, D.; Mukherjee, R. K. Magnetic Studies on Low-Spin $K_3Mn(CN)_6$. *J. Phys. Chem. Solids* **1979**, *40* (9), 691–695. https://doi.org/10.1016/0022-3697(79)90181-1.

110.   Wegeberg, C.; Wenger, O. S. Luminescent First-Row Transition Metal Complexes. *JACS Au* **2021**, *1* (11), 1860–1876. https://doi.org/10.1021/jacsau.1c00353.

111.   Herr, P.; Kerzig, C.; Larsen, C. B.; Häussinger, D.; Wenger, O. S. Manganese(I) Complexes with Metal-to-Ligand Charge Transfer Luminescence and Photoreactivity. *Nat. Chem.* **2021**, *13* (10), 956–962. https://doi.org/10.1038/s41557-021-00744-9.

112.   Dubicki, L.; Ferguson, J.; Krausz, E. R.; Lay, P. A.; Maeder, M.; Taube, H. Electronic Absorption and MCD Spectra of Mononuclear and Binuclear Complexes of Osmium(III) Ammines with π-Bonding Aromatic Ligands: Complexes with C_{2v} and D_{2h} Symmetry. *J. Phys. Chem.* **1984**, *88* (18), 3940–3941. https://doi.org/10.1021/j150662a011.

113.   Buhr, J. D.; Winkler, J. R.; Taube, H. Characterization and Reactions of Osmium(IV) Ammines. *Inorg. Chem.* **1980**, *19* (8), 2416–2425. https://doi.org/10.1021/ic50210a048.

114.   Jay, R. M.; Norell, J.; Eckert, S.; Hantschmann, M.; Beye, M.; Kennedy, B.; Quevedo, W.; Schlotter, W. F.; Dakovski, G. L.; Minitti, M. P.; Hoffmann, M. C.; Mitra, A.; Moeller, S. P.; Nordlund, D.; Zhang, W.; Liang, H. W.; Kunnus, K.; Kubiček, K.; Techert, S. A.; Lundberg, M.; Wernet, P.; Gaffney, K.; Odelius, M.; Föhlisch, A. Disentangling Transient Charge Density and Metal–Ligand Covalency in Photoexcited Ferricyanide with Femtosecond Resonant Inelastic Soft X-Ray Scattering. *J. Phys. Chem. Lett.* **2018**, *9* (12), 3538–3543. https://doi.org/10.1021/acs.jpclett.8b01429.

115.   Hendrickx, M. F. A.; Chibotaru, L. F.; Ceulemans, A. The Electronic Structure and Spectrum of $Mo(CN)_8^{3-}$. *Inorg. Chem.* **2003**, *42* (2), 590–597. https://doi.org/10.1021/ic0258734.

116.   Neese, F. The ORCA Program System. *WIREs Comput. Mol. Sci.* **2012**, *2* (1), 73–78. https://doi.org/10.1002/wcms.81.

117.   Perdew, J. P.; Ernzerhof, M.; Burke, K. Rationale for Mixing Exact Exchange with Density Functional Approximations. *J. Chem. Phys.* **1996**, *105* (22), 9982–9985. https://doi.org/10.1063/1.472933.

118.   Adamo, C.; Barone, V. Toward Reliable Density Functional Methods without Adjustable Parameters: The PBE0 Model. *J. Chem. Phys.* **1999**, *110* (13), 6158–6170. https://doi.org/10.1063/1.478522.

119.   Weigend, F.; Ahlrichs, R. Balanced Basis Sets of Split Valence, Triple Zeta Valence and Quadruple Zeta Valence Quality for H to Rn: Design and Assessment of Accuracy. *Phys Chem Chem Phys* **2005**, *7* (18), 3297–3305. https://doi.org/10.1039/B508541A.

120.   Weigend, F. Hartree–Fock Exchange Fitting Basis Sets for H to Rn. *J. Comput. Chem.* **2008**, *29* (2), 167–175. https://doi.org/10.1002/jcc.20702.

121.   Zhurko, G.A. and Zhurko, D.A. Chemcraft. Version 1.8 (Build 595). www.chemcraftprog.com

122.   Mingardi, M. A. P. Luminescence and Absorption Spectra of Some d6 Complexes. Ph.D. Dissertation, University of British Columbia, Vancouver, Canada, 1969. http://hdl.handle.net/2429/35663.

123.   Vogler, A.; Kunkely, H. Luminescence from Hexacyanoruthenate(III). *Inorganica Chim. Acta* **1981**, *53*, L215–L216. https://doi.org/10.1016/S0020-1693(00)84799-4.

124.   Englman, R.; Jortner, J. The Energy Gap Law for Radiationless Transitions in Large Molecules. *Mol. Phys.* **1970**, *18* (2), 145–164. https://doi.org/10.1080/00268977000100171.

125.   Dannöhl-Fickler, R.; Kelm, H.; Wasgestian, F. Solvent and Temperature Dependence of the Phosphorescence Decay Time of Hexacyanochromate(III). *J. Lumin.* **1975**, *10* (2), 103–112. https://doi.org/10.1016/0022-2313(75)90038-1.

126.   Adamson, A. W. Medium and Ligand Effects on the Absorption Spectra of Some Cr(III) Complexes. *J. Inorg. Nucl. Chem.* **1966**, *28* (9), 1955–1964. https://doi.org/10.1016/0022-1902(66)80286-5.

127.   Marchaj, A.; Wasgestian, F. Ligand Field Photolysis of $[Cr(CN)_6]^{3-}$ in Acetonitrile. *Inorganica Chim. Acta* **1985**, *102* (1), L13–L15. https://doi.org/10.1016/S0020-1693(00)89061-1.

128.   Castelli, Francesco.; Forster, L. S. Multiple Decays of Hexakis(Cyano-C)Chromate(3-) Emission in Rigid Glass Solutions. *J. Am. Chem. Soc.* **1973**, *95* (22), 7223–7226. https://doi.org/10.1021/ja00803a006.

129.   DeSimone, R. E. Electron Paramagnetic Resonance Studies of Low-Spin D5 Complexes. Trisbidentate Complexes of Iron(III), Ruthenium(III), and Osmium(III) with Sulfur-Donor Ligands. *J. Am. Chem. Soc.* **1973**, *95* (19), 6238–6244. https://doi.org/10.1021/ja00800a015.